Characterizing Precipitation Behaviors of H- in the Martian Atmosphere

Sarah A Henderson[1], Jasper S. Halekas[2], Rebecca Jolitz[3], David Mitchell[4], Christian Xavier Mazelle[5], Francis G. Eparvier[6], and Meredith K Elrod[7]

[1]Montana State University
[2]University of Iowa
[3]Laboratory of Atmospheric and Space Physics
[4]University of California, Berkeley
[5]IRAP; Université de Toulouse; CNRS; CNES; UPS-OMP; Toulouse, France
[6]LASP
[7]NASA Goddard Space Flight Center

April 16, 2024

Abstract

Solar wind protons can charge exchange with the extensive hydrogen corona of Mars, resulting in a significant flux of energetic neutral atoms (ENAs). As these solar wind hydrogen ENAs precipitate into the upper atmosphere, they can experience electron attachment or detachment, resulting in populations of H- and H+, respectively, with upstream velocity. We seek to characterize the behavior of H- in the ionosphere of Mars through a combination of in situ data analysis and mathematical models. Observations indicate that measurable H- precipitation in the ionosphere of Mars is rare, occurring during only 1.8% of available observations. These events occur primarily during high energy solar wind conditions near perihelion. We also compare H- fluxes to those of H+ and find that H- fluxes are 4.5 times less than H+, indicating preferential conversion of hydrogen ENAs to H+. We develop a simple model describing the evolution of the charged and neutral fraction of ENAs and H- ions versus altitude. We find that 0.29 - 0.78% of ENAs are converted to H- for solar wind energies 1 - 3 keV. We also predict that the effects of photodetachment on the H-H- system are non-negligible.

Characterizing Precipitation Behaviors of H^- in the Martian Atmosphere

Sarah Henderson[1,2], Jasper Halekas[1], Rebecca Jolitz[3], David Mitchell[3], Christian Mazelle[4], Frank Eparvier[5], Meredith Elrod[6,7]

[1]The University of Iowa, Iowa City, IA, USA
[2]Montana State University, Bozeman, MT, USA
[3]Space Sciences Laboratory, University of California Berkeley, Berkeley, CA, USA
[4]IRAP, Université de Toulouse, CNRS, UPS, CNES, Toulouse, France
[5]Laboratory for Atmospheric and Space Physics, University of Colorado, Boulder, CO, USA
[6]Planetary Environments Lab, Goddard Space Flight Center, NASA, Greenbelt, MD, USA
[7]CRESST II, University of Maryland, College Park, College Park, MD, USA

Key Points:

- H^- precipitation events at Mars occur primarily during high energy solar wind events during perihelion
- H^- fluxes are on average 4.5 times less than those of H^+, indicating preferential conversion of energetic neutral atoms to H^+
- Effects of photodetachment on H^- are notable at ionospheric altitudes above 125 km

Corresponding author: Sarah Henderson, `sarah.henderson5@montana.edu`

Abstract

Solar wind protons can charge exchange with the extensive hydrogen corona of Mars, resulting in a significant flux of energetic neutral atoms (ENAs). As these solar wind hydrogen ENAs precipitate into the upper atmosphere, they can experience electron attachment or detachment, resulting in populations of H^- and H^+, respectively, with upstream velocity. We seek to characterize the behavior of H^- in the ionosphere of Mars through a combination of in situ data analysis and mathematical models. Observations indicate that measurable H^- precipitation in the ionosphere of Mars is rare, occurring during only 1.8% of available observations. These events occur primarily during high energy solar wind conditions near perihelion. We also compare H^- fluxes to those of H^+ and find that H^- fluxes are $\sim$4.5 times less than H^+, indicating preferential conversion of hydrogen ENAs to H^+. We develop a simple model describing the evolution of the charged and neutral fraction of ENAs and H^- ions versus altitude. We find that 0.29 - 0.78% of ENAs are converted to H^- for solar wind energies 1 - 3 keV. We also predict that the effects of photodetachment on the H-H^- system are non-negligible.

Plain Language Summary

As the solar wind propagates throughout the solar system, it can directly interact with the atmosphere of Mars. Protons in the solar wind can obtain an electron from hydrogen in the planet's large atmosphere, resulting in a population of energetic neutral hydrogen atoms (ENAs). These ENAs bypass electromagnetic boundaries, penetrating into the collisional CO_2 component of the Martian atmosphere. Through interactions with CO_2, these ENAs can obtain or lose an electron, generating populations of H^- and H^+. We find that observing measurable amounts of H^- at Mars is rather difficult. These ions are best observed during high energy solar wind conditions during Mars's closest approach to the Sun. We also find that hydrogen ENAs are more often converted to H^+ than H^-. We also develop a simple mathematical model describing how many ENAs are converted to H^-. We find that in addition to collisional interactions with CO_2, interactions between solar radiation and H^- are non-negligible. We determine that a minute fraction of ENAs are converted to H^-.

1 Introduction

Mars is home to both a collisional CO_2 dominated atmosphere and an extensive hydrogen corona (Anderson Jr., 1974; Chaufray et al., 2008). As the solar wind propagates towards Mars, protons within the solar wind directly interact with hydrogen atoms within the planet's corona. These protons can charge exchange with neutral hydrogen, becoming energetic neutral atoms (ENAs) with upstream solar wind energies (Gunell et al., 2006; Holmström et al., 2002; Kallio et al., 1997). These ENAs bypass electromagnetic boundaries about Mars and penetrate to altitudes of $\sim$120 km. Along their path of propagation, these ENAs undergo three primary mechanisms: electron stripping, electron attachment, or excitation. These processes result in measurable populations of H^+ (Kallio & Barabash, 2001; Halekas et al., 2015), H^- (Halekas et al., 2015), and proton aurora (Deighan et al., 2018; Ritter et al., 2018).

Previous studies have explored numerous characteristics of this ENA population and its various byproducts in the atmosphere of Mars using in situ data (Brinkfeldt et al., 2006; Futaana et al., 2006a, 2006b; Gunell et al., 2006; Wang et al., 2013; Halekas et al., 2015; Halekas, 2017; Halekas et al., 2017; Deighan et al., 2018; Hughes et al., 2019; Henderson et al., 2021, 2022; Jones et al., 2022) as well as modeling techniques (Brecht, 1997; Kallio et al., 1997; Kallio & Barabash, 2001; Holmström et al., 2002; Kallio et al., 2006; V. I. Shematovich et al., 2011; Diéval et al., 2012; Wang et al., 2013; Bisikalo et al., 2018; Wang et al., 2018; V. Shematovich & Bisikalo, 2021; Hughes et al., 2023). More recent studies have focused on the behaviors of the charged byproducts of this population (H^+ and H^-) as a function of various spatial and temporal parameters (Halekas, 2017; Henderson et al., 2021, 2022; Jones et al., 2022).

The properties of H^-, in particular, have been left largely unexplored. One previous study examined how these particles' fluxes vary with respect to season, upstream solar wind energy, and how H^- densities compare to upstream solar wind protons and penetrating H^+ (Jones et al., 2022). In this manuscript, we seek to focus on the behaviors of H^- in the Martian atmosphere using a combination of in situ data and mathematical models. We examine data collected by the Mars Atmosphere and Volatile EvolutioN (MAVEN) spacecraft to determine under what conditions H^- is most often observed at Mars (Jakosky et al., 2015). We cross-compare the observed fluxes of H^- and H^+ as a function of atmospheric CO_2 column density. We then use a previous framework outlined in Halekas (2017) describing the evolution of the charge fraction of H^+ as a function of altitude to discuss the anticipated equilibrium behaviors of H^-. We develop a simple model describing the neutral and negative charge fractions of hydrogen ENAs and H^- by examining the effects of charge exchange, electron attachment, and photodetachment. Finally, we compare our modelling results to our data set.

2 H^- In Situ Observations

Before modeling the behavior of H^-, we are interested in characterizing how these particles behave in the Mars atmosphere by utilizing in situ data. We focus on isolating MAVEN observations where H^- and H^+ ions are present. The following sections describe how we obtain the H^- data, as well as under what conditions we most frequently observe this particle population. We also briefly compare how H^- and H^+ fluxes vary with respect to CO_2 column density.

2.1 Methodology

We begin by examining Solar Wind Ion Analyzer (SWIA) and Solar Wind Electron Analyzer (SWEA) L2 archive data collected during MAVEN dayside periapses at altitudes below 250 km between 2014 and 2023 (Halekas et al., 2015; D. Mitchell et al., 2016).

For each orbit, we determine if the Sun is within SWEA's and/or SWIA's field of view (FOV). Due to the position of both instruments on MAVEN in addition to the spacecraft's orbital configuration, the Sun may not necessarily be within the instruments' FOVs during each periapsis (Halekas et al., 2015; D. Mitchell et al., 2016). Depending on the orbital configuration, the Sun may only be observable by one of the instruments. In order to best detect both H^+ and H^-, it is critical that the instruments are pointed sunward since solar wind hydrogen ENAs are highly collimated in the antisunward direction. Once we confirm that the Sun is in the relevant instrument's FOV, we proceed to analyze the electron and ion data collected within that periapsis.

Due to low count statistics, we first determine an average background count rate for each orbit. We separate the electron data into backscattered and downward populations using the same methods described in Girazian and Halekas (2021). Namely, we determine the dot product between the electron's velocity vector and Mars surface normal for a given measurement. If the dot product is positive, this is considered backscattered; the opposite is true for the downward condition (Girazian & Halekas, 2021). Due to SWEA's position on MAVEN, specific anode bins are physically blocked by the spacecraft; we therefore exclude these bins from our analysis within the downward and backscattered data (D. Mitchell et al., 2016). Once these anodes are masked, we compute an angular sum to generate an energy-count profile for a given timestamp and repeat this process for each individual 8-second observation during a periapsis. We also implement an outlier rejection to the SWEA data to better isolate the H^- signal. It has been shown that magnetosheath electrons are able to precipitate into the upper Martian atmosphere under certain magnetic field configurations, resulting in "hot" electron signatures visible below altitudes of 250 km (D. L. Mitchell et al., 2001). To mitigate this, we sum the electron counts for energies above 600 eV in each time bin collected over a periapsis for both the backscattered and downward populations. Once we obtain total counts per time stamp in each direction, we find the median total counts for a given periapsis in each respective direction. Any timestamps where the total counts exceed 2.5 times the periapsis median is rejected. This threshold was chosen empirically after examining a multitude of periapses. We then proceed to sum over all timestamps for the duration of the periapsis for the backscattered data, resulting in an angular-averaged count-energy profile. From this total backscattered profile, we take the average number of counts in the three highest energy bins to generate an average background for a given periapsis.

Once this average background is obtained from the backscattered data, we turn to the downward propagating data. The main purpose of obtaining the background for each periapsis is two-fold: to determine whether the total H^- signal is statistically significant compared to that of the background and to perform a background subtraction. To determine if the H^- signal is significantly different from that of the background (BG), we first isolate the total core counts (C_{core}) that are collected at energies within $0.83E_{SW} \leq E_{SW} \leq 1.34E_{SW}$, where E_{SW} is the upstream solar wind energy for that particular orbit. This range of energies was chosen in order to encompass neighboring energy bins for SWEA, given that the instrument's resolution is 17% (D. Mitchell et al., 2016). We tailor this limit towards higher energies in order to prevent signals from low energy sources (i.e., Auger electrons) from dominating our signal.

We repeat these methods on the SWIA H^+ data with two subtle changes. For the hot population filter, we sum over energies above 200 eV; this range is imposed in order to eliminate potential spacecraft charging signatures while still detecting planetary ion populations or accelerated heavy ions (Halekas et al., 2017). The second change that we implement is the range of energies we examine in order to isolate each distribution's core points. We focus on energy bins that satisfy $0.855E_{SW} \leq E_{SW} \leq 1.29E_{SW}$; these limits were chosen due to SWIA's intrinsic resolution of 14.5% (Halekas et al., 2015).

Once we remove hot populations in both the H^- and H^+ data, we then compare the distribution of isolated core counts to the background counts of each population's signal. To do so, we compute a z-score using a right-tailed Z test,

$$z = \frac{\overline{C_{core}} - \overline{BG}}{\sqrt{(\sigma_{core}/\sqrt{N_{core}})^2 + (\sigma_{BG}/\sqrt{N_{BG}})^2}}, \quad (1)$$

where $\overline{C_{core}}$ is the average of the isolated core points, $\overline{BG}$ is the average of the background counts, σ_{core} is the standard deviation of the core counts, σ_{BG} is the standard deviation of the background counts, N_{core} is the number of core counts, and N_{BG} is the number of background counts. Note that these standard deviations are computed using Bessel's correction to account for bias in small population samples. We ultimately convert these z-scores into a more familiar p-value using a right-tailed test lookup table.

In addition to computing a z-score, we also compute a signal to noise ratio (SNR) for each periapsis. We implement this statistic as well after examining the distribution of p-scores for the H^- signals. To compute a SNR, we compare the core counts to those of the background. We find the peak total number of counts in the core of the distribution and take the ratio of this and the average background counts. After examining various orbits, we determine that a SNR ≥ 3 quantifies a statistically significant signal.

After repeating the above process for H^- and H^+ data, we conclude that further visual confirmation is needed to determine if an H^- signal is actually present. Figure 2 shows the distribution of SNRs and p-scores for the dayside orbits between 2014 and 2023 where data were available for SWEA and/or SWIA. We see a clear difference between

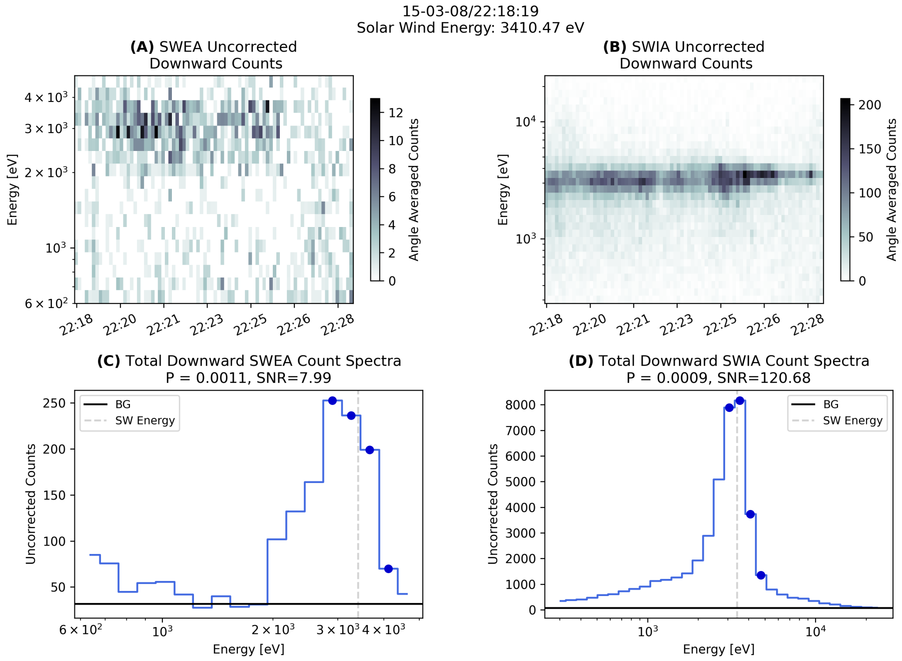

Figure 1. Example of SWEA and SWIA uncorrected count-energy spectra from a coronal mass ejection event on March 8, 2015. (A) Downward, angle summed count profile for SWEA without background correction. (B) Same as Panel A, but for SWIA. (C) Coadded SWEA orbital profile resulting from summing over all timestamps in Panel A. Blue points represent C_{core}. (D) Same as Panel C, but for SWIA. Note different scaling on each subpanel.

the two datasets; SWIA H^+ data are significantly more robust than SWEA H^- data. Of the 2,344 SWEA observations available, 1,708 (72.9%) had background levels that were higher than the core counts. Of SWIA's 4,247 available observations, only 186 (4.38%) demonstrated this behavior. When examining the distribution of orbits that satisfy what we deem as a statistically significant threshold (SNR $\geq$ 3 and p $\leq$ 0.05), we are left with 68 SWEA orbits and 2,761 SWIA orbits. Upon further inspection of numerous orbits, we find that the backscattered signal detected by SWEA in its highest energy bins is sometimes higher than anticipated. This skews the p-score and SNR to values outside of what we would nominally deem statistically significant, even if an H^- signal is indeed present. We also find that during orbits with upstream solar wind energy less than $\sim$1000 eV, the p-score and SNR are often skewed towards more statistically significant values due to high signals of Auger electrons contaminating the region where we anticipate H^- to be present. Because of these factors, we examine all available orbits by eye to determine if a signal is detected, an example of which can be seen in Figure 1. Once we visually confirm that an H^- signal is present within a given periapsis, we proceed to analyze each 8-second or 4-second slice of downward propagating H^- and H^+ data, respectively.

We compute an average background count rate for a given periapsis by dividing $\overline{BG}$ by the duration of the periapsis in seconds. We then apply a background correction to each energy-anode bin using this background count rate to try and eliminate instrument background and counts generated by high energy particles, such as cosmic rays. After applying this correction, we convert these background corrected counts into differential energy flux. We then sum over all anode bins to generate an angular-averaged profile for the downward population observed during each individual timestamp. This

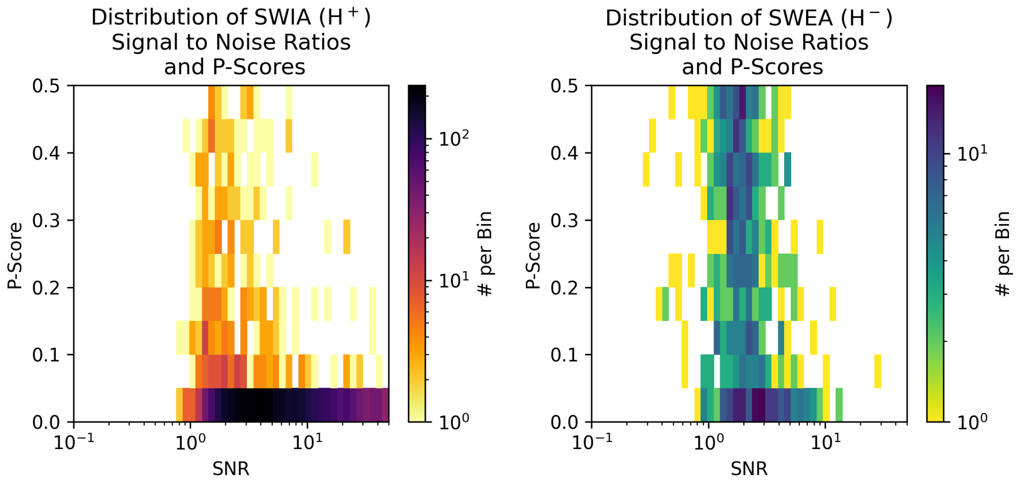

Figure 2. Distribution of p-scores and signal to noise ratios (SNRs) for SWIA and SWEA dayside periapses between 2014 and 2023. Note different scaling on colorbars.

process is repeated for both SWEA and SWIA data at an 8-second or 4-second cadence, respectively.

With the aforementioned energy restrictions, FOV constraints, L2 archive data availability, and visual confirmation, we are only left with 43 periapses to cross compare H^+ and H^-.

2.2 Results

We seek to compare the behavior of H^+ and H^- in the Martian atmosphere by examining temporal and spatial characteristics of their energy spectra. As is apparent from Figure 1, the flux of H^- is significantly lower than that of H^+ and other ion species within the Martian ionosphere. Particularly, the backscattered signal of H^- is extremely diminished; we therefore only examine downward propagating populations of H^+ and H^- in this analysis.

2.2.1 Distribution of H^- Detections

Since detection of H^- events is rare (1.8% of available orbits), we first want to determine under what conditions these particles are most frequently observed. Figure 3 summarizes the distribution of these orbits as a function of various relevant parameters.

We see a clear bias towards H^- events occurring near perihelion (L_S=251°) and during southern summer (270° $\leq L_S \leq$ 360°). This is not surprising, given the seasonal increase in the exposed hydrogen column density upstream of the Martian bow shock, which allows for an increased rate of ENA generation and consequent charge-changing processes (Halekas, 2017). Additionally, dust season occurs within southern summer; dust storms have been shown to sweep up water molecules to ionospheric altitudes, where they can undergo photodissociation (Chaffin et al., 2021). This process creates a larger source of hydrogen within the upper atmosphere of Mars, which may also aid in the creation of more H^- ions. In conjunction with a seasonal bias, we also observe a higher occurrence of H^- precipitation events for high solar wind energies. We would also anticipate this trend for two reasons: an increased cross section of interaction and easier discern-

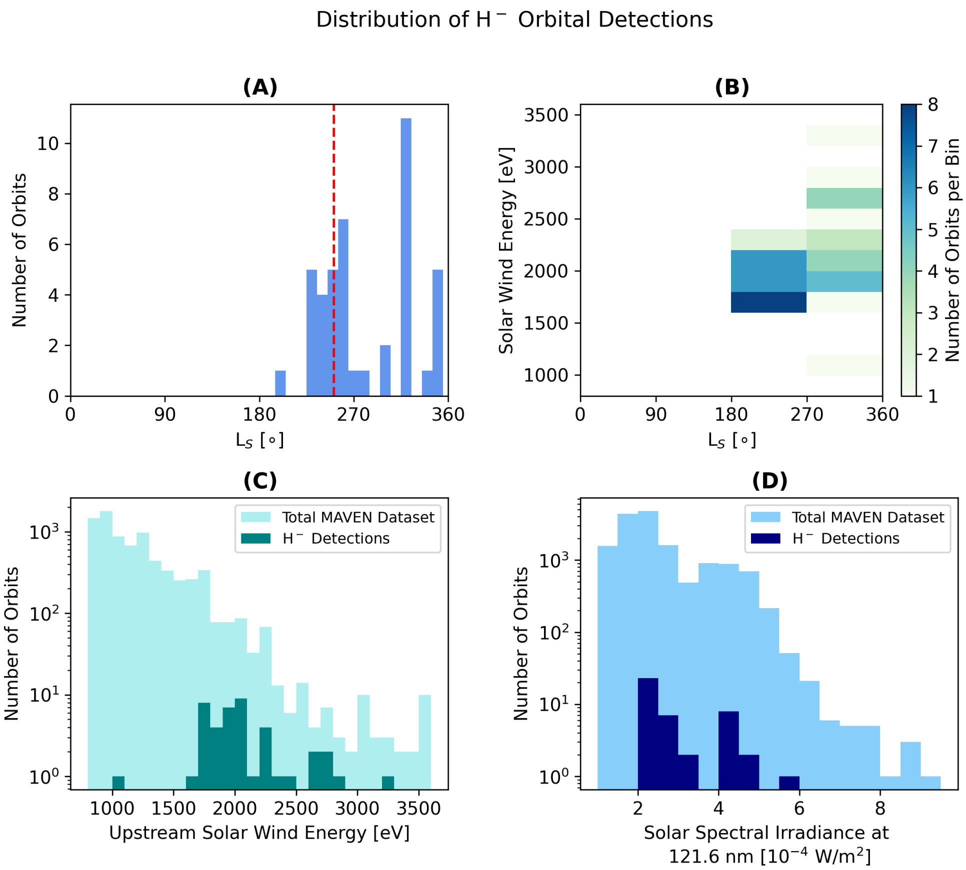

Figure 3. Distribution of orbits with H^- detections with respect to solar longitude (L_S), solar wind energy, and solar EUV irradiance. Red vertical line in Panel A indicates perihelion ($L_S = 251°$).

ment from other electron populations at Mars. The cross section for electron attachment increases significantly with increasing solar wind energy (Lindsay et al., 2005). Additionally, Auger and/or photoelectrons are not present at these higher energies, which also allows us to see H^- precipitation much more clearly.

Another potentially important factor affecting H^- precipitation is solar extreme ultraviolet (EUV) emission. Utilizing orbit-averaged L2 data from the Extreme Ultraviolet Monitor (EUVM) onboard MAVEN, we examine the distribution of H^- events as a function of solar Lyman-α emission (Eparvier et al., 2015). In Figure 3 Panels B and D, we do not see any strong correlation between H^- precipitation and solar EUV irradiance. Compared to the overall distribution of solar EUV irradiance measurements collected over the duration of the MAVEN mission, we do not see any particular bias in H^- detections towards high or low periods of solar flux. This indicates that H^- precipitation should occur throughout various points of the solar cycle, which is indeed what we observe in Figure 4.

From Figure 4A, we see that the majority of H^- detections are clustered in 2016 near perihelion during the declining phase of Solar Cycle 24. We also observe a second cluster of events in 2022 as we approach Solar Cycle 25 maximum, where the solar EUV input is ~2-3 times larger than during solar minimum. This distribution of events indicates that there is no strong correlation between solar cycle and observed H^- precipitation. Figure 4B summarizes the distribution of events as a function of solar EUV irradiance as well as solar wind energy. We see from this panel that events occurring during periods of lower EUV input are observed at a broader range of energies when compared to those that occur near solar maximum.

We also see in Figure 4A that all events prior to 2022 are primarily clustered near perihelion. This can most likely be attributed to the seasonal variability of the hydrogen corona; at perihelion, the exposed hydrogen column density upstream of the bow shock increases by a factor of ~3 compared to aphelion (Halekas, 2017). Having more hydrogen available upstream of the bow shock allows for a higher production rate of ENAs (up to ~5%), which ultimately allows for a higher likelihood of H^- and H^+ precipitation (Halekas, 2017).

The trends presented in Figures 3 and 4 seem to indicate that there is a "sweet-spot" for H^- precipitation in the upper atmosphere of Mars. We observe a bias in H^- precipitation events during high energy solar wind conditions, which often coincide with heightened periods of solar activity. We also observe most precipitation events near perihelion, where both the solar EUV irradiance and the amount of exposed hydrogen column density upstream of Mars's bow shock peak in the planet's orbit about the Sun. Shortly after perihelion, we observe an uptick in H^- precipitation events during southern summer solstice, which coincides with Mars's dust season. We also observe precipitation events at various points within the solar cycle, suggesting there is not a strong dependence of H^- precipitation on solar EUV emission. With all of these factors, it appears that there are a multitude of drivers that affect H^- precipitation. Our findings suggest a delicate balance between solar wind conditions, solar activity, and Martian atmospheric conditions is required in order to observe H^-. Further observations are required to better understand the behaviors presented here.

2.2.2 Column Density Variation

In addition to examining the distribution of H^- precipitation events, we also want to investigate the behavior of H^- and H^+ congruently as a function of atmospheric CO_2 column density. Using CO_2 data from the Neutral Gas and Ion Mass Spectrometer (NGIMS), we compute column density values for each 8-second SWEA and 4-second SWIA measurement within our 43 orbit sample (P. Mahaffy et al., 2015). To obtain each column density value, we trace the path of the precipitating solar wind hydrogen from the Sun

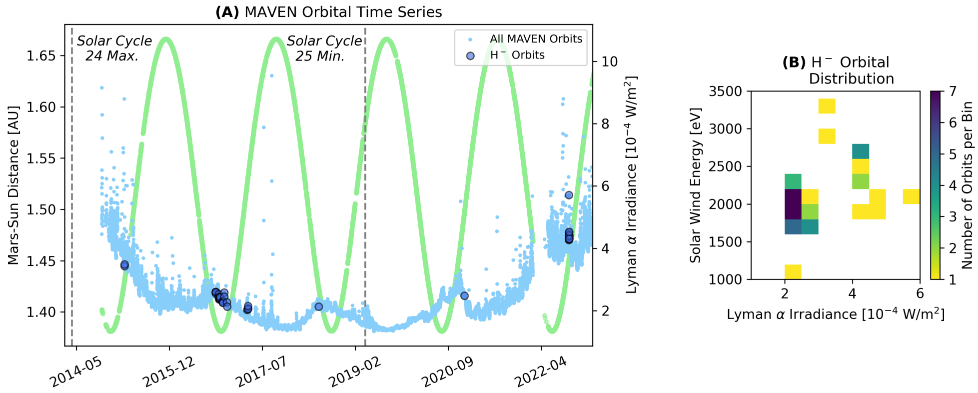

Figure 4. (A) Time series of orbit-averaged solar EUV irradiance from MAVEN Extreme Ultraviolet Monitor (EUVM) observations. Light blue points represent all orbit-averaged solar EUV irradiances, while dark blue points represent orbits where H^- was detected. Green points show the Mars-Sun distance in astronomical units, with the corresponding axis on the left-hand side of the figure. Solar cycle phases are indicated by the text and gray hashed lines. (B) Distribution of H^- orbits as a function of upstream solar wind energy and solar EUV irradiance. Note: The gap in data near April 2022 is due to MAVEN going into safe-mode.

to the point at which it is observed by MAVEN. Ultimately, this quantifies the amount of CO_2 that a given particle has passed through along its path of propagation. The exact details of this calculation are described in Henderson et al. (2021).

Previous studies have demonstrated that H^+ flux varies as a function of column density, increasing as hydrogen ENAs interact with more CO_2 molecules along their path of propagation. This behavior is exhibited up until a critical column density, where H^+ and H production reach an equilibrium; ultimately, a "turnover" in the flux profile is observed where collisional processes and consequential energy loss dominate (Halekas, 2017; Henderson et al., 2021). We anticipate a similar behavior demonstrated by H^-; however, the point at which this turnover occurs may vary due to different physical processes that result in the production/destruction of H^-. To investigate whether these behaviors are present within our H^- observations, we start by examining the average flux profiles of H^+ and H^- using all available orbital data.

Figure 5 summarizes the average behavior of precipitating H^+ and H^- fluxes as a function of CO_2 column density. We see in Panel A that H^+ fluxes increase steadily until $\sim 6\times10^{14}$ cm^{-2}, at which point they seemingly plateau. At 5.25×10^{15} cm^{-2}, we note a slight increase in the flux relative to this plateau and also see a dramatic falloff in the flux profile thereafter, decreasing by a factor of $\sim$4. We do not observe such stark behavior in Panel B. The H^- fluxes do not increase as rapidly with respect to column density as H^+. We note, however, that the H^- fluxes begin to plateau at $\sim 3\times10^{14}$ cm^{-2} and experience a smooth decline starting at 10^{16} cm^{-2}.

We see from Panels A and B that H^+ is much more favorably created through charge exchange than H^-, as indicated by nearly an order of magnitude difference in the average peak fluxes. This is reflected in Panel C, where we observe a peak flux ratio of $\sim$8. Across the entire range of column densities, H^+ flux is $\sim$4.5 times greater than that of H^-. Clearly, ENAs are preferentially converted to H^+ along their path of propagation;

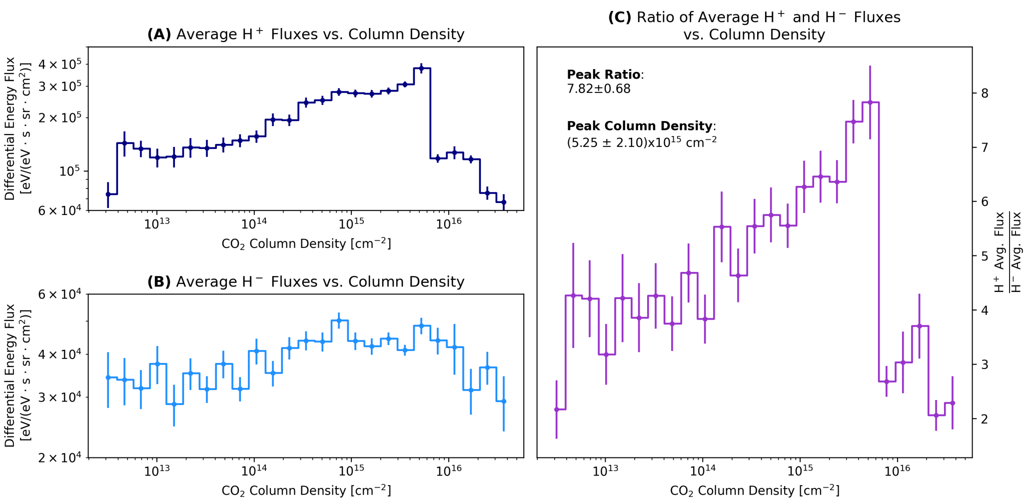

Figure 5. Average profiles of H^+ and H^- fluxes from 43 periapses. (A) Behavior of H^+ flux as a function of CO_2 column density. Mean is taken per column density bin, with the standard error of the mean shown as error bars. (B) Same as Panel A, but for H^-. Note different scaling. (C) Ratio of average H^+ and H^- fluxes versus CO_2 column density.

this is not surprising, given the magnitude of the cross sections for electron stripping versus electron attachment (Lindsay et al., 2005).

3 H^- Mathematical Model

Previously, Halekas (2017) constructed a simple model for charge equilibrium between H and H^+ by implementing cross sections for interactions between these two particle species and CO_2. They described the evolution of the charged (F^+) and neutral (F^0) fractions of these populations, respectively, as a function of altitude using a coupled set of differential equations. Utilizing the same framework, we can repeat this analysis for H^-.

When discussing the behavior of H^- in the atmosphere of Mars, we must consider three primary processes: electron attachment ($H + CO_2 \rightarrow H^- + CO_2^+$), charge exchange ($H^- + CO_2 \rightarrow H + CO_2^-$), and photodetachment ($H^- + \gamma \rightarrow H + e^-$). To most accurately represent the behavior of precipitating ENAs, one should compute a weighted sum over all of the various particle species that these hydrogen ENAs collide with in the upper atmosphere. However, for altitudes below 250 km, CO_2 comprises over $\sim$95% of the Martian atmosphere; thus, it is a reasonable first-order approximation that CO_2 is the dominant species with which ENAs and their charged byproducts can interact (Nier & McElroy, 1977; P. R. Mahaffy et al., 2015).

Following the framework of Halekas (2017), we can construct a coupled set of equations describing the evolution of ENAs and H^- as we progress through the Martian atmosphere. Accounting for charge exchange, electron attachment, and photodetachment, we arrive at the following,

$$\frac{dF^-}{dr} = [\sigma_{02}(E)F^0(r) - \sigma_{20}(E)F^-(r)]n_{CO_2}(r) - N_{PD}(r,E)F^-(r) \tag{2}$$

$$\frac{dF^0}{dr} = [\sigma_{20}(E)F^-(r) - \sigma_{02}(E)F^0(r)]n_{CO_2}(r) + N_{PD}(r,E)F^-(r), \tag{3}$$

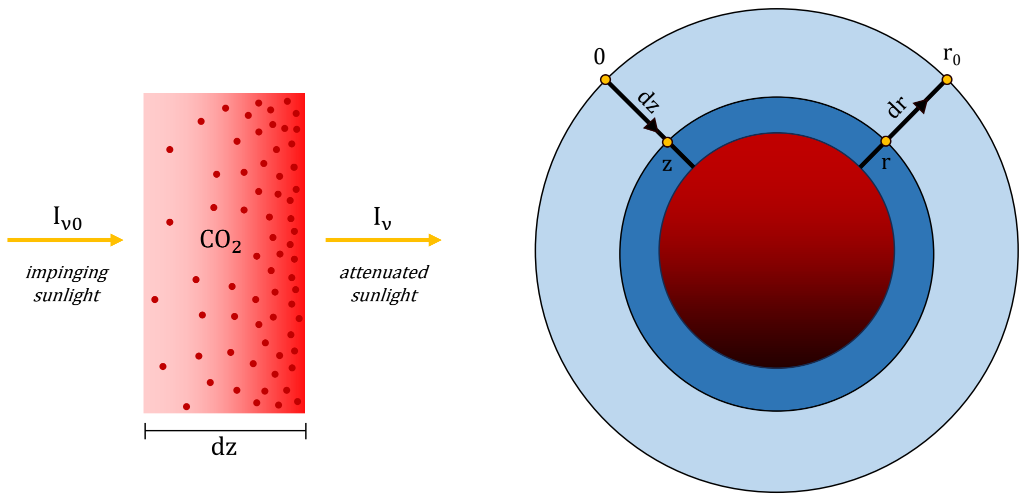

Figure 6. Outline of set up for photodetachment calculation. Left figure shows sunlight ($I_{\nu 0}$) hitting CO_2 slab. Attenuated light (I_ν) displayed on right side of slab. Right figure outlines the coordinates implemented in this calculation, with Mars at the center in burgundy. Yellow points show location of integration limits.

where F^- is the fraction of precipitating hydrogen ENAs converted to H^-, F^0 is the fraction of H^- converted to ENAs, n_{CO_2} is the CO_2 number density, r is altitude, σ_{02} is the cross section for electron attachment of H by CO_2, σ_{20} is the cross section for charge exchange of H^- with CO_2, and N_{PD} represents the number of photodetachments over a unit distance. We do not include the effects of H^+ charge exchange with CO_2 in this system, which can alter F^0 by 4 - 15% (Halekas, 2017); this is left for future examination. The charge exchange and electron attachment terms within Equations 2 and 3 are well characterized; however, we need to derive the photodetachment term, N_{PD}.

3.1 Photodetachment Term Derivation

To determine the number of interactions an impinging particle experiences over a given time, we can write the following expression,

$$k = n\sigma v, \tag{4}$$

where n is the number density of the target particle species, σ is the cross section of the given interaction, and v is the velocity of the impinging particle. This can be easily rewritten as an interaction rate per unit length if we simply divide Equation 4 by the incoming particle's velocity, v. Examining the first two terms on the right-hand side of Equations 2 and 3, we can see that the units of these terms are congruent with k/v. Therefore, we can determine the rate of photodetachment and divide this by the velocity of H^- in order to determine the number of photodetachments that occur over a given unit length (N_{PD}).

To do this, we first need to determine how solar light is attenuated by the CO_2 dominated Martian atmosphere. This will help us to characterize the rate of photodetachment as a function of altitude as CO_2 density varies. Assuming we have sunlight impinging on a slab of CO_2, we can write a basic set of equations describing how the flux of solar photons varies with respect to the thickness of the CO_2 slab (or rather, altitude). Figure 6 outlines the set up of this problem.

From basic radiative processes, we can write the following,

$$\frac{dI_\nu(\nu, z)}{dz} = -n_{CO_2}(z)\sigma(\nu)I_\nu(\nu, z), \tag{5}$$

where I_ν is the specific intensity of light, dz is the thickness of the CO_2 slab, n_{CO_2} is the number density, ν is the frequency of light, and σ is the cross section of a given interaction between the incoming photons and CO_2. In principle, the cross section term should encompass all possible chemical processes, including collisional excitation, absorption, and emission. However, we only include photoabsorption (σ_{PA}) by CO_2 to simplify our model.

Integrating Equation 5 using the limits described in Figure 6, we arrive at the following,

$$\int \frac{dI_\nu(\nu, r)}{I_\nu(\nu, r)} = -\int_r^{r_0} \sigma_{PA}(\nu)n_{CO_2}(r')\ dr'. \tag{6}$$

We can define an expression for atmospheric column density,

$$N_{COL} \equiv \int_r^{r_0} n_{CO_2}(r')\, dr.' \tag{7}$$

Utilizing this definition, the integral on the right-hand side of Equation 6 can simply be expressed as a function of column density,

$$\int \frac{dI_\nu(\nu, r)}{I_\nu(\nu, r)} = -\sigma_{PA}(\nu)N_{COL}. \tag{8}$$

Evaluating Equation 8 leads to a solution for I_ν,

$$I_\nu(\nu, N_{COL}) = I_{\nu 0}(\nu)e^{-\sigma_{PA}(\nu)N_{COL}}, \tag{9}$$

where $I_{\nu 0}(\nu)$ is the solar specific intensity at the top of the Martian atmosphere. Solar specific intensity is conserved as a function of distance and is well described by the Planck function for a blackbody emitting at T = 5,800 K. Naturally, the solar spectrum is not a perfect blackbody, as has been shown by previous studies (Huebner et al., 1992; Huebner & Mukherjee, 2015). However, we utilize this assumption in our calculation to simplify our mathematical model. With all of these moving parts and substituting for energy, we can finally write I_E as a function of photon energy, blackbody temperature, and column density,

$$I_E(E, T, N_{COL}) = \left(\frac{2E^3}{c^2h^2}\frac{1}{e^{E/kT}-1}\right)e^{-\sigma_{PA}(E)N_{COL}}. \tag{10}$$

As previously mentioned, we seek to quantify the photodetachment rate at a given point within the Martian atmosphere in order to characterize the fraction of H^- converted to H due to photodetachment. Now that we have determined how solar radiation is attenuated by CO_2, we can proceed to calculate the photodetachment rate.

The photodetachment rate can be written in the following way,

$$k = \int_{\Omega_0}^{\Omega_f} d\Omega \int_{E_0}^{\infty} \frac{I_E(E, T, N_{COL})}{E \cdot h}\sigma_{PD}(E)dE, \tag{11}$$

where Ω is the solid angle, and σ_{PD} is the photodetachment cross section (McLaughlin et al., 2017). Substituting Equation 10 into 11, we arrive at the following,

$$k = \int_{\Omega_0}^{\Omega_f} d\Omega \int_{E_0}^{\infty} \sigma_{PD}(E)\left(\frac{2E^2}{c^2h^3}\frac{1}{e^{E/kT}-1}\right)e^{-\sigma_{PA}(E)N_{COL}}dE. \tag{12}$$

Using simple geometry, we can write the total solid angle through which the solar radiation passes,

$$\Omega = 4\theta cos(\pi/2 - \theta), \tag{13}$$

where $\theta = \arctan(R_\odot/d_{MS})$, $R_\odot$ is the radius of the Sun, and d_{MS} is Mars-Sun distance. If we evaluate Equation 13 using Mars-Sun distances for aphelion and perihelion, we obtain $\Omega = [3.1112 \cdot 10^{-5}\ , 4.5221 \cdot 10^{-5}]$ steradians, respectively.

Combining Equations 12 and 13, we arrive at our final solution describing the rate of photodetachment at a given CO_2 column density in the Martian atmosphere,

$$k = 4\theta cos(\pi/2 - \theta) \int_{E_0}^{\infty} \sigma_{PD}(E) \left(\frac{2E^2}{c^2h^3} \frac{1}{e^{E/kT} - 1} \right) e^{-\sigma_{PA}(E)N_{COL}} dE. \tag{14}$$

We can see from Equation 14 that there are still two undefined parameters: $\sigma_{PD}(E)$ and $\sigma_{PA}(E)$. These variables quantify photodetachment and photoabsorption cross sections, respectively, and do not have analytical forms. We therefore implement measured values of these parameters across various photon energies to obtain a numerical solution for k (Chandrasekhar, 1945; Branscomb & Smith, 1955; Sun & Weissler, 1955; Smith & Burch, 1959; Cairns & Samson, 1965; Conrath et al., 1973; Wishart, 1979; Craver, 1982; Lewis & Carver, 1983; Rahman & Hird, 1986; Yoshino et al., 1996; Parkinson et al., 2003; Stark et al., 2007; McLaughlin et al., 2017).

One aspect to note is the temperature dependence of the photoabsorption cross sections utilized in this study. As we progress through the Martian atmosphere, the temperature profile varies. In the case of CO_2 in the range of altitudes we examine, the temperature varies from approximately 180 K to 245 K (Stone et al., 2018). The photoabsorption cross sections utilized in our calculations were obtained at a temperature of 195 K; thus, our photodetachment rate will be an approximation based on the assumption that CO_2 photoabsorption cross sections do not vary significantly with temperature.

We can determine k by implementing the various measured cross sections for photodetachment and photoabsorption. To do so, we integrate Equation 12 over energies where photodetachment cross sections are nonzero. From Supplemental Figure S1, we see that the relevant energy ranges fall between the near infrared and EUV. Previous measurements have demonstrated that Martian atmospheric transmittance of solar photons is most impeded by CO_2 in the infrared at wavelengths between $\sim$2 and 13 μm (Conrath et al., 1973). If we examine Supplemental Figure S1, we find that these near infrared wavelengths are outside the domain where photodetachment is prevalant. The infrared photoabsorption cross sections are therefore irrelevant, since the photodetachment cross section tends towards zero in this frequency range. We do note, however, that there is an overlap in photoabsorption and photodetachment in the EUV regime and proceed to evaluate Equation 14 over this frequency range.

Integrating Equation 14 over energies $\sim 10^{-1} - 10^{5}$ eV, we obtain a photodetachment rate that depends only on Mars-Sun distance. Upon evaluating Equation 14 for column densities $10^{9} - 10^{18}$ cm^{-2} for a given Mars-Sun distance, we observe a (9.25×10^{-6})% change in the photodetachment rate between the maximum and minimum column density. This indicates that attenuation due to CO_2 photoabsorption is negligible, and thus the column density dependence in Equation 14 can be neglected.

With these results, we can further simplify Equation 14. If we set the photoabsorption term ($e^{-\sigma_{PA}(E)N_{COL}}$) to unity and integrate over all EUV energies, our integrand simplifies to 2.0244×10^{5} s^{-1} sr^{-1}. We can now express the rate of photodetachment in the following manner,

$$k = (2.0244 \times 10^{5}) \left[4\theta cos(\pi/2 - \theta)\right]. \tag{15}$$

Evaluating the above equation during aphelion and perihelion results in photodetachment rates of $\sim$6 and $\sim$9 per second, respectively. This is in relatively good agreement with photodetachment rates obtained in previous studies using measured solar photon flux at 1 AU (Huebner et al., 1992; Desai et al., 2021). Extrapolating the results from these studies to Mars (i.e., 1.3814 - 1.666 AU) results in rates between $\sim$5 and $\sim$7 photodetachments per second, which is congruent with our derivation.

If we recall Equation 4, we can now write $N_{PD} = k/v_{H^-} = k\sqrt{m_{H^-}/2E}$, where m_{H^-} is the mass of H^-. This allows us to write a full expression describing the behavior of hydrogen ENAs and H^- as they interact with both solar photons and the Martian atmosphere:

$$\frac{dF^-}{dr} = [\sigma_{02}(E)F^0(r) - \sigma_{20}(E)F^-(r)]n_{CO_2}(r) - (2.0244 \times 10^5)\,[4\theta cos(\pi/2-\theta)]\sqrt{\frac{m_{H^-}}{2E}}F^-(r) \quad (16)$$

$$\frac{dF^0}{dr} = [\sigma_{20}(E)F^-(r) - \sigma_{02}(E)F^0(r)]n_{CO_2}(r) + (2.0244 \times 10^5)\,[4\theta cos(\pi/2-\theta)]\sqrt{\frac{m_{H^-}}{2E}}F^-(r). \quad (17)$$

3.2 Numerical and Analytical Solutions

Before explicitly solving Equations 16 and 17, we can examine how the number of interactions per unit length for electron attachment, charge exchange, and photodetachment varies with respect to CO_2 atmospheric density by quantifying each coefficient within these coupled differential equations. Utilizing the cross sections for electron attachment and charge exchange collected between 1 and 3 keV, we can calculate the quantity of each coefficient within Equations 16 and 17 and determine at which point within the Martian atmosphere a given process dominates (Nakai et al., 1987; Lindsay et al., 2005). Figure 7 summarizes how these three processes vary with respect to altitude using this approach.

It is important to note that the cross section for charge exchange between H^- and CO_2 has not been measured within the energy range we examine here. Previous studies have utilized O_2 cross sections to generate proxy cross sections for CO_2 when measurements were not available (Kallio & Barabash, 2000, 2001). We employ this method in our analysis as well.

Nakai et al. (1987) measured the cross section of charge exchange between H^- and O_2 for energies spanning 1 eV to 10 MeV. They also measured the cross section of charge exchange between H^- and CO_2 (σ_{20} in our analysis), but only at energies greater than 20 keV. In order to extrapolate σ_{20} to solar wind energies, we employ a scaling factor. We average the ratio of the O_2 cross section to the CO_2 cross section in the 20 keV to 10 MeV range. We then multiply the entire O_2 cross section profile by this average ratio to obtain proxy values of σ_{20} at energies pertinent for our analysis here (Nakai et al., 1987).

We observe a few interesting behaviors in Figure 7. First and foremost, we see in Panels A and B that charge exchange is the primary process governing H^- for altitudes below 194 $\pm$ 5 km across various energies and Mars-Sun distances. Above this threshold, however, we note that photodetachment overtakes both electron attachment and charge exchange processes. Further examination of Panel A indicates that the altitude range at which electron attachment overtakes photodetachment is much lower than that of charge exchange. Panel B shows that photodetachment remains significantly important compared to electron attachment at altitudes above 134 $\pm$ 8 km. This feature becomes most important at perihelion for low energy solar wind conditions. Figure 7 indicates that photodetachment becomes relatively negligible at ionospheric altitudes below $\sim$125 km. However, in the upper ionosphere, it appears that this H^- sink cannot be ignored.

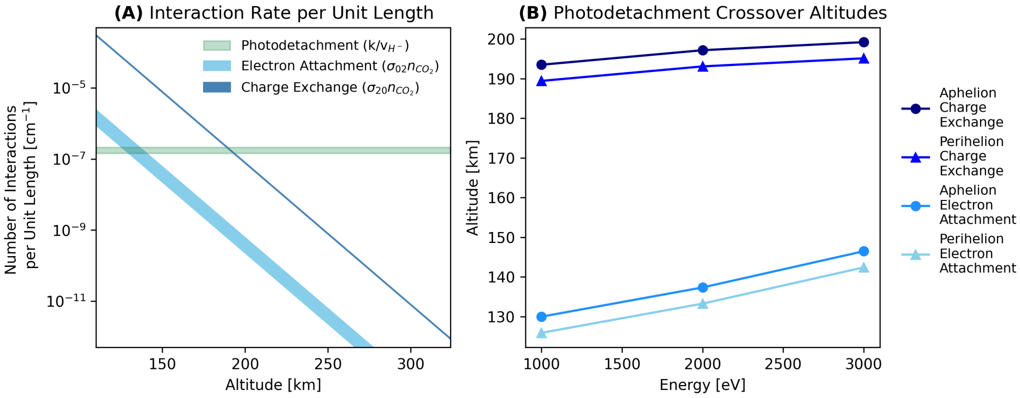

Figure 7. Summary of interactions per unit length for charge exchange, electron attachment, and photodetachment. (A) The upper bound for electron attachment was determined using cross sections at 3 keV, while the lower bound was determined using 1 keV cross sections. The inverse of this applies to the charge exchange curve. The upper bound of the photodetachment curve represents the value at perihelion for $E_{H^-} = 1$ keV, while the lower bound is at aphelion. The altitude values and corresponding density values were calculated using the average CO_2 profile from Supplemental Figure S2. (B) Summary of altitudes at which photodetachment becomes dominated by either charge exchange or electron attachment (i.e., where the blue regions overlap the green region in Panel A). Curves are separated by Mars-Sun distance and relevant process, as indicated in legend.

3.2.1 Analytical Solution Derivation

For altitudes below 125 km, we can find an approximate solution to Equations 16 and 17 by assuming k $\rightarrow$ 0. This leaves us with differential equations in the following form,

$$\frac{dF^-}{dr} = [\sigma_{02}F^0(r) - \sigma_{20}F^-(r)]n_{CO_2}(r) \tag{18}$$

$$\frac{dF^0}{dr} = [\sigma_{10}F^-(r) - \sigma_{01}F^0(r)]n_{CO_2}(r). \tag{19}$$

If we add Equations 18 and 19, we find that $\frac{dF^-}{dr} = -\frac{dF^0}{dr}$. This, combined with the boundary conditions of $F^-(\infty) = 0$ and $F^0(\infty) = 1$, results in

$$F^0(r) = 1 - F^-(r). \tag{20}$$

We can write the density in Equations 18 and 19 analytically if we assume that the atmosphere is in equilibrium. This is true for altitudes below 300 km in the Martian atmosphere, which is approximately the upper limit of the altitudes we examine here (Cravens et al., 2017). We can write the CO_2 density profile in an exponential form,

$$n_{CO_2}(r) = N_0 e^{mr}, \tag{21}$$

where N_0 is a reference CO_2 number density, and the magnitude of m is the inverse of the atmospheric scale height. Substituting Equations 20 and 21 into Equation 18, we are left with a differential equation in the following form:

$$\frac{dF^-}{dr} + (\sigma_{02} + \sigma_{20})N_0 e^{mr} - \sigma_{02}N_0 e^{mr} = 0. \tag{22}$$

Equation 22 has a solution for the negative charge fraction,

$$F^{-}(r) = \frac{\sigma_{02}}{\sigma_{02} + \sigma_{20}} \left[1 - e^{\frac{-N_0(\sigma_{02}+\sigma_{20})}{m} e^{mr}}\right]. \tag{23}$$

Recalling Equation 7, we can rewrite the argument of the exponent in Equation 23 as a function of CO_2 column density. Substituting Equation 7 into Equation 23 and utilizing Equation 20 to solve for $F^0(r)$, we arrive at approximate analytic solutions for the negative and neutral fractions,

$$F^{-}(r) = \frac{\sigma_{02}}{\sigma_{02} + \sigma_{20}} \left[1 - e^{-(\sigma_{02}+\sigma_{20})N_{COL}}\right] \tag{24}$$

$$F^{0}(r) = \frac{\sigma_{20}}{\sigma_{02} + \sigma_{20}} \left[1 + \frac{\sigma_{02}}{\sigma_{20}} e^{-(\sigma_{02}+\sigma_{20})N_{COL}}\right]. \tag{25}$$

If we assume that precipitating solar wind hydrogen atoms reach approximate equilibrium after one e-folding scale, we can determine from Equations 24 and 25 the equilibrium charge fraction, neutral fraction, and column density. Utilizing this assumption, we arrive at an equilibrium column density,

$$CD_{eq} = \frac{1}{\sigma_{02} + \sigma_{20}}. \tag{26}$$

The negative and neutral fractions converge over ∼5 e-folding scales to a final value expressed by the following equations,

$$F_f^{-} \simeq \frac{\sigma_{02}}{\sigma_{02} + \sigma_{20}} \tag{27}$$

$$F_f^{0} \simeq \frac{\sigma_{20}}{\sigma_{02} + \sigma_{20}}. \tag{28}$$

The electron stripping and charge exchange cross sections vary with respect to the energy of the incoming particle; thus, depending on upstream solar wind conditions, we would anticipate precipitating solar wind hydrogen to reach equilibrium at different column densities within the Martian atmosphere. Using NGIMS CO_2 data, we can explicitly obtain the fit parameters in Equation 21 that describe the average CO_2 density profile as a function of altitude to accurately evaluate Equations 24 and 25. The results of this fitting procedure on inbound verified CO_2 data can be seen in Supplemental Figure S2. These fit parameters, N_0 and m, are then implemented in our column density calculation.

3.2.2 Analytical and Numerical Solution Comparison

As we progress through the atmosphere, we expect the solutions to Equations 16 and 17 to converge to Equations 24 and 25, respectively. However, to understand the role that photodetachment plays at altitudes above 125 km, we can find precise solutions to Equations 16 and 17 across various solar wind energies and Mars-Sun distances using numerical integration methods[1]

Examining the numerical solution for F^- in Figure 8, we find that the maximum charge fraction is 0.78% for high energy solar wind conditions. For lower energy solar wind conditions, this decreases to 0.29%. Kallio et al. (1997) demonstrated that 1-3%

[1] These equations were solved using NDSolve in Mathematica with altitude bounds of 100 - 500 km. The boundary conditions were approximated at an altitude of 500 km. The values of N_0 and m implemented in these calculations can be found in Supplemental Figure S2.

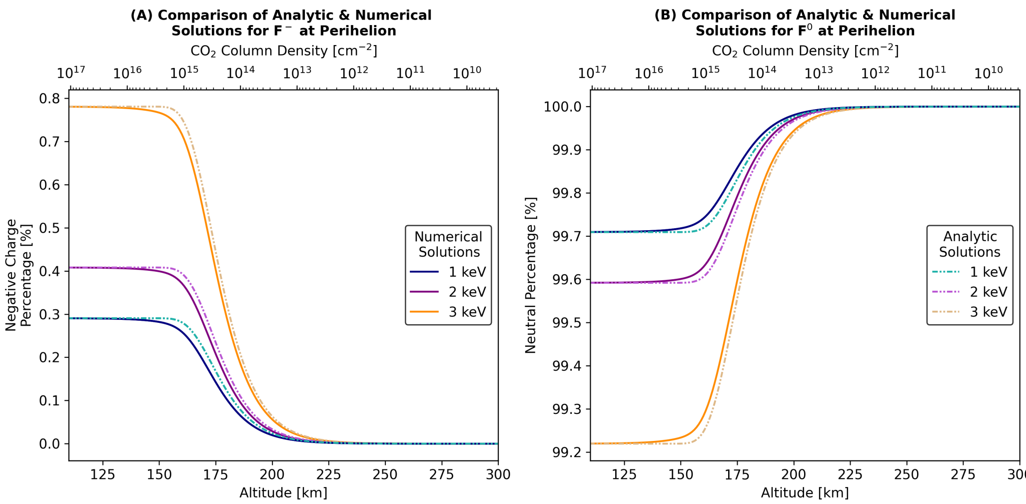

Figure 8. Summary of numerical and analytical solutions for F^- and F^0 at perihelion. Numerical solutions (solid) are obtained from Equations 16 and 17. Analytic solutions (dashed-dotted) are obtained from Equations 24 and 25.

of solar wind protons are converted to ENAs for the energy range we examine here. Combining this with the observed charge fractions determined from our model, this implies that we would anticipate observing 0.0029 - 0.023% of the upstream solar wind proton flux in the form of H^- ions.

Figure 8 summarizes the numerical and analytical solutions across various solar wind energies at perihelion for F^- and F^0. We only examine the results at perihelion since the numerical model does not change significantly as a function of Mars-Sun distance (see Supplemental Figure S3). We see in both panels that there is a slight divergence between the numerical and analytical solutions at altitudes between 130 and 200 km. We find that the fraction of ENAs converted to H^- is slightly lower in the numerical model compared to the analytical model, suggesting that photodetachment is playing a role in depleting the H^- population. If we examine these plots more carefully, we find that the maximum percent difference between the numerical and analytical charge fractions is 1 - 7%. For typical solar wind fluxes ($\sim 10^8$ cm^{-2} s^{-1}), we would anticipate a flux of H^- on the order of $\sim 10^3$ - 10^4 cm^{-2} s^{-1}. In order to detect the effects of photodetachment, we would need to be able to measure fluctuations of ~ 10 - 10^3 cm^{-2} s^{-1}. With SWEA's sensitivity, we would not be able to observe these differences; higher flux H^- events would be required to detect any deviations.

In general, H^- is not preferentially generated in the Martian environment due to the fact that it is so energetically unfavorable. We find that photodetachment dominates the H-H^- system in the upper ionosphere, while atmospheric collisional processes primarily govern these particles below 200 km. We observe a slight difference between our modeling results when photodetachment is included versus when it is excluded. We see a minute increase in the ENAs generated from this process. In practice, this difference would be extremely difficult to observe given our current instrumentation. Only during high energy solar wind conditions would we potentially be able to see the changes in the negative charge fraction induced by photodetachment.

4 Data-Model Comparison

We can now directly compare our observational results from Section 2 to our modeling results from Section 3. Below we will discuss how various aspects of our mathematical model compare to the MAVEN observations previously discussed.

We find that there is not a clear difference in the observed charge fractions as a function of Mars-Sun distance as shown in Supplemental Figure S3, indicating that H^- should be observed throughout various points within the Martian orbit. Figures 3 and 4 indicate that H^- is, however, preferentially observed near perihelion. This is not necessarily contradictory of our model; we do not incorporate variable conditions within the hydrogen corona or lower atmosphere in our framework. Previous studies have found that there is a clear seasonal (and consequently, Mars-Sun distance) dependence on the observed ENA and H^+ flux due to a factor of 3 increase in the exposed hydrogen column density (Halekas et al., 2015; Halekas, 2017). This expansion of the corona creates a larger deposition of ENAs, increasing the likelihood of conversion to H^+ and H^- within the CO_2 atmosphere. It has also been shown that the Martian atmosphere heats and consequently expands during southern summer, affecting hydrogen deposition and CO_2 densities (Halekas et al., 2015; Halekas, 2017; Hughes et al., 2019). These factors would also affect our numerical solutions, shifting them to higher altitudes at perihelion versus aphelion.

Revisiting the trends presented in Figure 4, we observe H^- precipitation at various points within the solar cycle. In principle, we would expect solar EUV emission to affect our observations due to the influence of photodetachment. However, Figure 8 demonstrates the charge fraction is only slightly influenced by this process at altitudes below 200 km. Figure 8 clearly shows that the primary factor at play is the upstream solar wind energy, which greatly impacts the observed charge fraction. Figure 3 bolsters this fact, showing that H^- events are distributed across various solar conditions but occur most often during high energy solar wind conditions.

Additionally, we can directly compare observed number fluxes of the upstream solar wind with those of downstream H^- to determine if the limiting charge fractions that we found in our model align well with observations. We implement the solar wind proxy data for each of our 43 orbits and determine the number flux using the given parameters. In order to compute the density of H^- and H^+ for a given measurement, we utilize the downward, background-corrected differential energy fluxes that we compute in Section 2.1. We then implement Equation 29 for each available measurement,

$$n = \sqrt{\frac{m}{2}}\Delta\Omega \sum_{i=1}^{n} E_i^{-3/2}\Delta E_i F(E_i), \tag{29}$$

where m is the mass of hydrogen, $\Delta\Omega$ is the solid angle, ΔE is the energy channel resolution, E is the energy, $F(E)$ is the differential energy flux, and i is the index of a given energy channel. For the SWEA data, we compute this sum for energies above 800 eV to best isolate H^- from other high flux populations (Jones et al., 2022). We repeat this computation for SWIA for energies spanning 300 to 4,000 eV in order to exclude spacecraft charging signatures in addition to pickup ions. Figure 9 summarizes our findings.

Recalling from Section 3.2.2, we anticipate 0.04 - 0.45% of upstream solar wind protons to be converted to H^+ (Halekas, 2017) and 0.0029 - 0.0234% to H^-. Panels B and C summarize the observed conversion efficiency for these populations, respectively. We see in Panel B that the conversion rate from solar wind protons to downstream H^+ is $\sim$0.8% across all energies, which is higher than the aforementioned anticipated limits. However, if we increase these limits by a factor of 3 to account for expansion of the hydrogen corona at perihelion (hashed region in Figure 9B), we find that the observed conversion rate aligns well with the model outlined in Halekas (2017). If we now look at the corresponding results in Panel C for H^-, we observe a $\sim$0.1% conversion rate, which is much higher than our derived limits. We do observe slight overlap between the lower limit

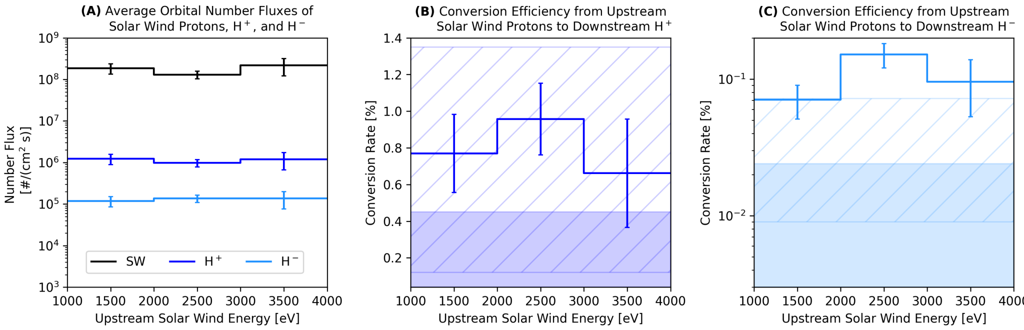

Figure 9. Summary of solar wind, H^+, and H^- orbital fluxes and corresponding conversion rates. (A) Orbit-averaged number fluxes for upstream solar wind protons (black), downstream H^+ (blue), and downstream H^- (light blue). Errorbars correspond to the standard error of the mean for a given bin. (B) Percent of solar wind protons converted to H^+. (C) Percent of solar wind protons converted to H^-. Shaded regions in B and C represent the percentage ranges based on our computations in Section 3.2.2 and previous findings (Kallio et al., 1997; Halekas, 2017). Hashed regions represent anticipated percentages at perihelion.

of our observations and the upper limit of the conversion rate at perihelion. This discrepancy between our model and observations may stem from an overestimation of σ_{20}. Smaller values of σ_{20} would result in larger values of F^- across all solar wind energies. Further investigation is required to better understand this behavior, and direct measurements of σ_{20} at solar wind energies would be extremely beneficial.

Examining Equation 26, we find that the turnover column densities for H^- and H^+ span $(3.068 \pm 0.059)\times10^{14}$ cm^{-2} and $(6.426 \pm 0.140)\times10^{14}$ cm^{-2} for energies falling between 1 and 3 keV, respectively (Nakai et al., 1987; Lindsay et al., 2005; Halekas, 2017). Comparing these values to the observed trends in Figure 5, we see that the observed profiles for both particle populations begin to plateau at these aforementioned column density values. This indicates that H^+ and H^- do approximately equilibrate after one e-folding scale, as was estimated by Equation 26.

We can also compare the observed abundance of H^+ with respect to H^- to what we would expect given the conversion rate of ENAs to each particle species. In Figure 5, we note that the peak ratio of H^+ to H^- fluxes in Panel C is $\sim$8. From our analysis in Section 3.2.2, we can determine the anticipated ratio of H^+ flux to H^- flux. We predicted that 0.29 - 0.78% of ENAs are converted to H^-, while Halekas (2017) determined that 4 - 15% of ENAs are converted to H^+. Using these limits, we can anticipate H^+ to be $\sim$13 - 19 times more abundant than H^-. These values are $\sim$2 times higher than the maximum observed ratio in Figure 5. This discrepancy is not surprising, given the conversion rates obtained in Figure 9. From our observations, we would anticipate a H^+/H^- ratio of $\sim$10, which is more in line with what we observe in Figure 5.

5 Summary

Using MAVEN data, we determine under what conditions H^- is best observed and compare fluxes of H^- and H^+ as a function of CO_2 column density. Using various methods, we isolate orbits with H^- signatures and determine that precipitation of this particle population is incredibly rare (1.8% of available observations). We also find that these particles are best observed during periods of high energy solar wind near perihelion; more of these events may become observable by MAVEN as we approach solar maximum, during which high energy solar events (i.e., CIRs, SIRs, CMEs) become more frequent. We observe no clear correlation between solar EUV irradiance or solar cycle with H^- observations. Lastly, we find that H^+ is preferentially generated from precipitating solar wind hydrogen ENAs compared to H^-. On average, H^+ fluxes are 4.5 times greater than observed H^- fluxes as a function of CO_2 column density.

We develop a simple model describing the equilibrium conditions for H^- in the Martian atmosphere by building off of a framework previously constructed by Halekas (2017). We consider the effects of charge exchange, electron attachment, and photodetachment in our model. We find numerical solutions for the charge (F^-) and neutral fractions (F^0) and determine the converging charge fraction to span 0.29 - 0.78% depending on upstream solar wind energy. We do not observe a significant change in the numerical solutions for F^- or F^0 between perihelion and aphelion. We find that the maximum difference between the analytical and numerical solutions when photodetachment is incorporated is 1 - 7%, occurring between 125 and 250 km.

When comparing our model to observations, we find good agreement in the equilibrium column densities for H^- and H^+. We observe a slight discrepancy in the observed charge fraction of H^- compared to our model, which underestimates our observations. We also find that the ratio of observed H^+/H^- fluxes is smaller than anticipated with our given model parameters. Further observations of H^- are needed to better understand the discrepancies discussed here.

Future work could compare the conditions under which we observe H^-, H^+, and proton aurora at Mars. Determining the distribution of these events will help us to better understand the Mars-solar wind interaction, as well as the primary factors governing the precipitation of hydrogen ENAs. The model describing H^- precipitation could also be expanded upon, accounting for hydrogen depletion caused by H^+ charge exchange with CO_2, seasonal variability of the hydrogen corona, as well as solar zenith angle dependencies. These two latter parameters greatly affect observed hydrogen deposition at Mars and are worth investigating (Halekas, 2017; Henderson et al., 2021; Hughes et al., 2019, 2023). It would also be of great scientific value to obtain direct measurements of electron stripping of H^- by CO_2 at solar wind energies to better constrain these processes as well.

6 Open Research

All MAVEN data utilized in this project are available on the NASA Planetary Data System. MAVEN SWIA data can be found here: `https://pds-ppi.igpp.ucla.edu/mission/MAVEN/MAVEN/SWIA`. MAVEN NGIMS data are available here: `https://pds-ppi.igpp.ucla.edu/mission/MAVEN/MAVEN/NGIMS`. MAVEN EUVM data are located here: `https://pds-ppi.igpp.ucla.edu/mission/MAVEN/MAVEN/EUV`. MAVEN SWEA data can be found at the following link: `https://pds-ppi.igpp.ucla.edu/mission/MAVEN/MAVEN/SWEA`. Photodetachment cross section data were curated by McLaughlin et al. (2017). Photoabsorption cross sections were obtained from multiple sources and can be found compiled at Henderson et al. (2023). Electron attachment cross sections can be found in Lindsay et al. (2005), and H^- charge exchange cross sections obtained in Section 3.2 can be found at Henderson et al. (2023). Solar wind data can also be found at Henderson et al. (2023).

Acknowledgments

The authors would like to acknowledge the MAVEN contract for support. We would also like to thank Dr. Casey DeRoo and Dr. Steve Spangler for their insightful conversations throughout this project.

References

Anderson Jr., D. E. (1974). Mariner 6, 7, and 9 Ultraviolet Spectrometer Experiment: Analysis of hydrogen Lyman alpha data. *Journal of Geophysical Research (1896-1977)*, *79*(10), 1513-1518. doi: https://doi.org/10.1029/JA079i010p01513

Bisikalo, D. V., Shematovich, V. I., Gérard, J.-C., & Hubert, B. (2018). Monte Carlo Simulations of the Interaction of Fast Proton and Hydrogen Atoms with the Martian Atmosphere and Comparison With In Situ Measurements. *Journal of Geophysical Research: Space Physics*, *123*(7), 5850-5861. doi: https://doi.org/10.1029/2018JA025400

Branscomb, L. M., & Smith, S. J. (1955, May). Experimental cross section for photodetachment of electrons from h^- and d^-. *Phys. Rev.*, *98*, 1028–1034. doi: 10.1103/PhysRev.98.1028

Brecht, S. H. (1997). Solar wind proton deposition into the Martian atmosphere. *Journal of Geophysical Research: Space Physics*, *102*(A6), 11287-11294. doi: https://doi.org/10.1029/97JA00561

Brinkfeldt, K., Gunell, H., Brandt, P. C., Barabash, S., Frahm, R., Winningham, J., … Dierker, C. (2006). First ENA observations at Mars: Solar-wind ENAs on the nightside. *Icarus*, *182*(2), 439-447. (Results from the Mars Express ASPERA-3 Investigation) doi: https://doi.org/10.1016/j.icarus.2005.12.023

Cairns, R. B., & Samson, J. A. R. (1965). Absorption and photoionization cross sections of co2, co, ar, and he at intense solar emission lines. *Journal of Geophysical Research (1896-1977)*, *70*(1), 99-104. doi: https://doi.org/10.1029/JZ070i001p00099

Chaffin, M. S., Kass, D. M., Aoki, S., Fedorova, A. A., Deighan, J., Connour, K., … Korablev, O. I. (2021, October). Martian water loss to space enhanced by regional dust storms. *Nature Astronomy*, *5*, 1036-1042. doi: 10.1038/s41550-021-01425-w

Chandrasekhar, S. (1945, September). On the Continuous Absorption Coefficient of the Negative Hydrogen Ion. *The Astrophysical Journal*, *102*, 223. doi: 10.1086/144755

Chaufray, J., Bertaux, J., Leblanc, F., & Quémerais, E. (2008). Observation of the hydrogen corona with SPICAM on Mars Express. *Icarus*, *195*(2), 598-613. doi: https://doi.org/10.1016/j.icarus.2008.01.009

Conrath, B., Curran, R., Hanel, R., Kunde, V., Maguire, W., Pearl, J., … Burke, T. (1973). Atmospheric and surface properties of mars obtained by infrared spectroscopy on mariner 9. *Journal of Geophysical Research (1896-1977)*, *78*(20), 4267-4278. doi: https://doi.org/10.1029/JB078i020p04267

Cravens, T. E., Hamil, O., Houston, S., Bougher, S., Ma, Y., Brain, D., & Ledvina, S. (2017). Estimates of ionospheric transport and ion loss at Mars. *Journal of Geophysical Research: Space Physics*, *122*, 10626–10637. doi: https://doi.org/10.1002/2017JA024582

Craver, C. D. (1982). *The coblentz society desk book of infrared spectra.* (2nd ed. ed.). Kirkwood, MO: The Society.

Deighan, J., Jain, S. K., Chaffin, M. S., Fang, X., Halekas, J. S., Clarke, J. T., … Jakosky, B. M. (2018, July). Discovery of a proton aurora at Mars. *Nature Astronomy*, *2*, 802-807. doi: 10.1038/s41550-018-0538-5

Desai, R. T., Zhang, Z., Wu, X., & Lue, C. (2021, may). Photodetachment and test-particle simulation constraints on negative ions in solar system plasmas. *The Planetary Science Journal*, *2*(3), 99. doi: 10.3847/PSJ/abf638

Diéval, C., Kallio, E., Barabash, S., Stenberg, G., Nilsson, H., Futaana, Y., … Brain, D. A. (2012). A case study of proton precipitation at Mars: Mars Express observations and hybrid simulations. *Journal of Geophysical Research: Space Physics*, *117*(A6). doi: https://doi.org/10.1029/2012JA017537

Eparvier, F., Chamberlin, P., & Woods, T. (2015). The Solar Extreme Ultraviolet

Monitor for MAVEN. *Space Sci Rev*, *195*, 293–301. doi: https://doi.org/10.1007/s11214-015-0195-2

Futaana, Y., Barabash, S., Grigoriev, A., Holmström, M., Kallio, E., Brandt, P. C., ... Dierker, C. (2006a). First ENA observations at Mars: ENA emissions from the Martian upper atmosphere. *Icarus*, *182*(2), 424-430. (Results from the Mars Express ASPERA-3 Investigation) doi: https://doi.org/10.1016/j.icarus.2005.09.019

Futaana, Y., Barabash, S., Grigoriev, A., Holmström, M., Kallio, E., Brandt, P. C., ... Dierker, C. (2006b). First ENA observations at Mars: Subsolar ENA jet. *Icarus*, *182*(2), 413-423. (Results from the Mars Express ASPERA-3 Investigation) doi: https://doi.org/10.1016/j.icarus.2005.08.024

Girazian, Z., & Halekas, J. (2021). Precipitating Solar Wind Hydrogen at Mars: Improved Calculations of the Backscatter and Albedo With MAVEN Observations. *Journal of Geophysical Research: Planets*, *126*(2), e2020JE006666. (e2020JE006666 2020JE006666) doi: https://doi.org/10.1029/2020JE006666

Gunell, H., Brinkfeldt, K., Holmström, M., Brandt, P. C., Barabash, S., Kallio, E., ... Dierker, C. (2006). First ENA observations at Mars: Charge exchange ENAs produced in the magnetosheath. *Icarus*, *182*(2), 431-438. (Results from the Mars Express ASPERA-3 Investigation) doi: https://doi.org/10.1016/j.icarus.2005.10.027

Halekas, J. S. (2017). Seasonal variability of the hydrogen exosphere of Mars. *Journal of Geophysical Research: Planets*, *122*(5), 901-911. doi: https://doi.org/10.1002/2017JE005306

Halekas, J. S., Lillis, R. J., Mitchell, D. L., Cravens, T. E., Mazelle, C., Connerney, J. E. P., ... Ruhunusiri, S. (2015). MAVEN observations of solar wind hydrogen deposition in the atmosphere of Mars. *Geophysical Research Letters*, *42*(21), 8901-8909. doi: https://doi.org/10.1002/2015GL064693

Halekas, J. S., Ruhunusiri, S., Harada, Y., Collinson, G., Mitchell, D. L., Mazelle, C., ... Jakosky, B. M. (2017). Structure, dynamics, and seasonal variability of the Mars-solar wind interaction: MAVEN Solar Wind Ion Analyzer in-flight performance and science results. *Journal of Geophysical Research: Space Physics*, *122*(1), 547-578. doi: https://doi.org/10.1002/2016JA023167

Halekas, J. S., Taylor, E. R., Dalton, G., Johnson, G., Curtis, D. W., McFadden, J. P., ... Jakosky, B. M. (2015). The Solar Wind Ion Analyzer for MAVEN. *Space Science Reviews*, *195*(1-4), 125-151. doi: 10.1007/s11214-013-0029-z

Henderson, S., Halekas, J., Girazian, Z., Espley, J., & Elrod, M. (2022). Influence of Magnetic Fields on Precipitating Solar Wind Hydrogen at Mars. *Geophysical Research Letters*, *49*(12), e2022GL099114. (e2022GL099114 2022GL099114) doi: https://doi.org/10.1029/2022GL099114

Henderson, S., Halekas, J., Jolitz, R., Mitchell, D., Mazelle, C., Eparvier, F., & Elrod, M. (2023). *MAVEN H^- Data (2014-2023).* Zenodo. doi: 10.5281/zenodo.8422352

Henderson, S., Halekas, J., Lillis, R., & Elrod, M. (2021). Precipitating Solar Wind Hydrogen as Observed by the MAVEN Spacecraft: Distribution as a Function of Column Density, Altitude, and Solar Zenith Angle. *Journal of Geophysical Research: Planets*, *126*(7), e2020JE006725. (e2020JE006725 2020JE006725) doi: https://doi.org/10.1029/2020JE006725

Holmström, M., Barabash, S., & Kallio, E. (2002). Energetic neutral atoms at Mars 1. Imaging of solar wind protons. *Journal of Geophysical Research: Space Physics*, *107*(A10). doi: https://doi.org/10.1029/2001JA000325

Huebner, W. F., Keady, J. J., & Lyon, S. P. (1992, September). Solar Photo Rates for Planetary Atmospheres and Atmospheric Pollutants. , *195*(1), 1-294. doi: 10.1007/BF00644558

Huebner, W. F., & Mukherjee, J. (2015, February). Photoionization and photodissociation rates in solar and blackbody radiation fields. , *106*, 11-45. doi:

10.1016/j.pss.2014.11.022

Hughes, A., Chaffin, M., Mierkiewicz, E., Deighan, J., Jain, S., Schneider, N., ... Jakosky, B. (2019). Proton Aurora on Mars: A Dayside Phenomenon Pervasive in Southern Summer. *Journal of Geophysical Research: Space Physics*, *124*(12), 10533-10548. doi: https://doi.org/10.1029/2019JA027140

Hughes, A., Chaffin, M., Mierkiewicz, E., Deighan, J., Jolitz, R., Kallio, E., ... Hegyi, B. (2023). Advancing Our Understanding of Martian Proton Aurora through a Coordinated Multi-Model Comparison Campaign. *Journal of Geophysical Research: Space Physics*.

Jakosky, B., Lin, R., & Grebowsky, J. e. a. (2015). The Mars Atmosphere and Volatile Evolution (MAVEN) Mission. *Space Science Reviews*, *195*, 3-48. doi: https://doi.org/10.1007/s11214-015-0139-x

Jones, N., Halekas, J., Girazian, Z., Mitchell, D., & Mazelle, C. (2022). MAVEN Observations of H^- Ions in the Martian Atmosphere. *Journal of Geophysical Research: Planets*, *127*(6), e2021JE006999. (e2021JE006999 2021JE006999) doi: https://doi.org/10.1029/2021JE006999

Kallio, E., & Barabash, S. (2000). On the elastic and inelastic collisions between precipitating energetic hydrogen atoms and martian atmospheric neutrals. *Journal of Geophysical Research: Space Physics*, *105*(A11), 24973-24996. doi: https://doi.org/10.1029/2000JA900077

Kallio, E., & Barabash, S. (2001). Atmospheric effects of precipitating energetic hydrogen atoms on the Martian atmosphere. *Journal of Geophysical Research: Space Physics*, *106*(A1), 165-177. doi: https://doi.org/10.1029/2000JA002003

Kallio, E., Barabash, S., Brinkfeldt, K., Gunell, H., Holmström, M., Futaana, Y., ... Dierker, C. (2006). Energetic Neutral Atoms (ENA) at Mars: Properties of the hydrogen atoms produced upstream of the martian bow shock and implications for ENA sounding technique around non-magnetized planets. *Icarus*, *182*(2), 448-463. (Results from the Mars Express ASPERA-3 Investigation) doi: https://doi.org/10.1016/j.icarus.2005.12.019

Kallio, E., Luhmann, J. G., & Barabash, S. (1997). Charge exchange near Mars: The solar wind absorption and energetic neutral atom production. *Journal of Geophysical Research: Space Physics*, *102*(A10), 22183-22197. doi: https://doi.org/10.1029/97JA01662

Lewis, B., & Carver, J. (1983). Temperature dependence of the carbon dioxide photoabsorption cross section between 1200 and 1970 Å. *Journal of Quantitative Spectroscopy and Radiative Transfer*, *30*(4), 297-309. doi: https://doi.org/10.1016/0022-4073(83)90027-4

Lindsay, B. G., Yu, W. S., & Stebbings, R. F. (2005, Mar). Cross sections for charge-changing processes involving kilo-electron-volt H and H^+ with CO and CO_2. *Phys. Rev. A*, *71*, 032705. doi: 10.1103/PhysRevA.71.032705

Mahaffy, P., Benna, M., & King, T. e. a. (2015). The Neutral Gas and Ion Mass Spectrometer on the Mars Atmosphere and Volatile Evolution Mission. *Space Science Reviews*, *195*, 49-73. doi: https://doi.org/10.1007/s11214-014-0091-1

Mahaffy, P. R., Benna, M., Elrod, M., Yelle, R. V., Bougher, S. W., Stone, S. W., & Jakosky, B. M. (2015). Structure and composition of the neutral upper atmosphere of Mars from the MAVEN NGIMS investigation. *Geophysical Research Letters*, *42*(21), 8951-8957. doi: https://doi.org/10.1002/2015GL065329

McLaughlin, B. M., Stancil, P. C., Sadeghpour, H. R., & Forrey, R. C. (2017, may). H photodetachment and radiative attachment for astrophysical applications. *Journal of Physics B: Atomic, Molecular and Optical Physics*, *50*(11), 114001. doi: 10.1088/1361-6455/aa6c1f

Mitchell, D., Mazelle, C., & Sauvaud, J. e. a. (2016). The MAVEN Solar Wind Electron Analyzer. *Space Science Reviews*, *200*, 495-528. doi: https://doi.org/10.1007/s11214-015-0232-1

Mitchell, D. L., Lin, R. P., Mazelle, C., Rème, H., Cloutier, P. A., Connerney,

J. E. P., … Ness, N. F. (2001). Probing Mars' crustal magnetic field and ionosphere with the MGS Electron Reflectometer. *Journal of Geophysical Research: Planets*, *106*(E10), 23419-23427. doi: https://doi.org/10.1029/2000JE001435

Nakai, Y., Shirai, T., Tabata, T., & Ito, R. (1987). Cross sections for charge transfer of hydrogen atoms and ions colliding with gaseous atoms and molecules. *Atomic Data and Nuclear Data Tables*, *37*(1), 69-101. doi: https://doi.org/10.1016/0092-640X(87)90005-2

Nier, A. O., & McElroy, M. B. (1977). Composition and structure of Mars' Upper atmosphere: Results from the neutral mass spectrometers on Viking 1 and 2. *Journal of Geophysical Research (1896-1977)*, *82*(28), 4341-4349. doi: https://doi.org/10.1029/JS082i028p04341

Parkinson, W., Rufus, J., & Yoshino, K. (2003). Absolute absorption cross section measurements of co2 in the wavelength region 163–200 nm and the temperature dependence. *Chemical Physics*, *290*(2), 251-256. doi: https://doi.org/10.1016/S0301-0104(03)00146-0

Rahman, F., & Hird, B. (1986). Electron detachment atomic cross sections from negative ions. *Atomic Data and Nuclear Data Tables*, *35*(1), 123-183. doi: https://doi.org/10.1016/0092-640X(86)90029-X

Ritter, B., Gérard, J.-C., Hubert, B., Rodriguez, L., & Montmessin, F. (2018). Observations of the proton aurora on mars with spicam on board mars express. *Geophysical Research Letters*, *45*(2), 612-619. doi: https://doi.org/10.1002/2017GL076235

Shematovich, V., & Bisikalo, D. (2021). A Kinetic Model for Precipitation of Solar-Wind Protons into the Martian Atmosphere. *Astronomy Reports*, *65*, 869-875. doi: https://doi.org/10.1134/S106377292110036X

Shematovich, V. I., Bisikalo, D. V., Diéval, C., Barabash, S., Stenberg, G., Nilsson, H., … Gérard, J.-C. (2011). Proton and hydrogen atom transport in the Martian upper atmosphere with an induced magnetic field. *Journal of Geophysical Research: Space Physics*, *116*(A11). doi: https://doi.org/10.1029/2011JA017007

Smith, S. J., & Burch, D. S. (1959, Feb). Photodetachment cross section of the negative hydrogen ion. *Phys. Rev. Lett.*, *2*, 165–166. doi: 10.1103/PhysRevLett.2.165

Stark, G., Yoshino, K., Smith, P., & Ito, K. (2007). Photoabsorption cross section measurements of co2 between 106.1 and 118.7nm at 295 and 195k. *Journal of Quantitative Spectroscopy and Radiative Transfer*, *103*(1), 67-73. doi: https://doi.org/10.1016/j.jqsrt.2006.07.001

Stone, S. W., Yelle, R. V., Benna, M., Elrod, M. K., & Mahaffy, P. R. (2018). Thermal Structure of the Martian Upper Atmosphere From MAVEN NGIMS. *Journal of Geophysical Research: Planets*, *123*(11), 2842-2867. doi: https://doi.org/10.1029/2018JE005559

Sun, H., & Weissler, G. L. (1955, 12). Absorption Cross Sections of Carbon Dioxide and Carbon Monoxide in the Vacuum Ultraviolet. *The Journal of Chemical Physics*, *23*(9), 1625-1628. doi: 10.1063/1.1742398

Wang, X.-D., Alho, M., Jarvinen, R., Kallio, E., Barabash, S., & Futaana, Y. (2018). Precipitation of Hydrogen Energetic Neutral Atoms at the Upper Atmosphere of Mars. *Journal of Geophysical Research: Space Physics*, *123*(10), 8730-8748. doi: https://doi.org/10.1029/2018JA025188

Wang, X.-D., Barabash, S., Futaana, Y., Grigoriev, A., & Wurz, P. (2013). Directionality and variability of energetic neutral hydrogen fluxes observed by Mars Express. *Journal of Geophysical Research: Space Physics*, *118*(12), 7635-7642. doi: https://doi.org/10.1002/2013JA018876

Wishart, A. W. (1979, November). The bound-free photodetachment cross section of h-. *Journal of Physics B: Atomic and Molecular Physics*, *12*(21), 3511. doi: 10.1088/0022-3700/12/21/009

Yoshino, K., Esmond, J., Sun, Y., Parkinson, W., Ito, K., & Matsui, T. (1996). Absorption cross section measurements of carbon dioxide in the wavelength region 118.7–175.5 nm and the temperature dependence. *Journal of Quantitative Spectroscopy and Radiative Transfer*, *55*(1), 53-60. doi: https://doi.org/10.1016/0022-4073(95)00135-2

Characterizing Precipitation Behaviors of H^- in the Martian Atmosphere

Sarah Henderson[1,2], Jasper Halekas[1], Rebecca Jolitz[3], David Mitchell[3], Christian Mazelle[4], Frank Eparvier[5], Meredith Elrod[6,7]

[1]The University of Iowa, Iowa City, IA, USA
[2]Montana State University, Bozeman, MT, USA
[3]Space Sciences Laboratory, University of California Berkeley, Berkeley, CA, USA
[4]IRAP, Université de Toulouse, CNRS, UPS, CNES, Toulouse, France
[5]Laboratory for Atmospheric and Space Physics, University of Colorado, Boulder, CO, USA
[6]Planetary Environments Lab, Goddard Space Flight Center, NASA, Greenbelt, MD, USA
[7]CRESST II, University of Maryland, College Park, College Park, MD, USA

Key Points:

- H^- precipitation events at Mars occur primarily during high energy solar wind events during perihelion
- H^- fluxes are on average 4.5 times less than those of H^+, indicating preferential conversion of energetic neutral atoms to H^+
- Effects of photodetachment on H^- are notable at ionospheric altitudes above 125 km

---

Corresponding author: Sarah Henderson, `sarah.henderson5@montana.edu`

Abstract

Solar wind protons can charge exchange with the extensive hydrogen corona of Mars, resulting in a significant flux of energetic neutral atoms (ENAs). As these solar wind hydrogen ENAs precipitate into the upper atmosphere, they can experience electron attachment or detachment, resulting in populations of H^- and H^+, respectively, with upstream velocity. We seek to characterize the behavior of H^- in the ionosphere of Mars through a combination of in situ data analysis and mathematical models. Observations indicate that measurable H^- precipitation in the ionosphere of Mars is rare, occurring during only 1.8% of available observations. These events occur primarily during high energy solar wind conditions near perihelion. We also compare H^- fluxes to those of H^+ and find that H^- fluxes are $\sim$4.5 times less than H^+, indicating preferential conversion of hydrogen ENAs to H^+. We develop a simple model describing the evolution of the charged and neutral fraction of ENAs and H^- ions versus altitude. We find that 0.29 - 0.78% of ENAs are converted to H^- for solar wind energies 1 - 3 keV. We also predict that the effects of photodetachment on the H-H^- system are non-negligible.

Plain Language Summary

As the solar wind propagates throughout the solar system, it can directly interact with the atmosphere of Mars. Protons in the solar wind can obtain an electron from hydrogen in the planet's large atmosphere, resulting in a population of energetic neutral hydrogen atoms (ENAs). These ENAs bypass electromagnetic boundaries, penetrating into the collisional CO_2 component of the Martian atmosphere. Through interactions with CO_2, these ENAs can obtain or lose an electron, generating populations of H^- and H^+. We find that observing measurable amounts of H^- at Mars is rather difficult. These ions are best observed during high energy solar wind conditions during Mars's closest approach to the Sun. We also find that hydrogen ENAs are more often converted to H^+ than H^-. We also develop a simple mathematical model describing how many ENAs are converted to H^-. We find that in addition to collisional interactions with CO_2, interactions between solar radiation and H^- are non-negligible. We determine that a minute fraction of ENAs are converted to H^-.

1 Introduction

Mars is home to both a collisional CO_2 dominated atmosphere and an extensive hydrogen corona (Anderson Jr., 1974; Chaufray et al., 2008). As the solar wind propagates towards Mars, protons within the solar wind directly interact with hydrogen atoms within the planet's corona. These protons can charge exchange with neutral hydrogen, becoming energetic neutral atoms (ENAs) with upstream solar wind energies (Gunell et al., 2006; Holmström et al., 2002; Kallio et al., 1997). These ENAs bypass electromagnetic boundaries about Mars and penetrate to altitudes of $\sim$120 km. Along their path of propagation, these ENAs undergo three primary mechanisms: electron stripping, electron attachment, or excitation. These processes result in measurable populations of H^+ (Kallio & Barabash, 2001; Halekas et al., 2015), H^- (Halekas et al., 2015), and proton aurora (Deighan et al., 2018; Ritter et al., 2018).

Previous studies have explored numerous characteristics of this ENA population and its various byproducts in the atmosphere of Mars using in situ data (Brinkfeldt et al., 2006; Futaana et al., 2006a, 2006b; Gunell et al., 2006; Wang et al., 2013; Halekas et al., 2015; Halekas, 2017; Halekas et al., 2017; Deighan et al., 2018; Hughes et al., 2019; Henderson et al., 2021, 2022; Jones et al., 2022) as well as modeling techniques (Brecht, 1997; Kallio et al., 1997; Kallio & Barabash, 2001; Holmström et al., 2002; Kallio et al., 2006; V. I. Shematovich et al., 2011; Diéval et al., 2012; Wang et al., 2013; Bisikalo et al., 2018; Wang et al., 2018; V. Shematovich & Bisikalo, 2021; Hughes et al., 2023). More recent studies have focused on the behaviors of the charged byproducts of this population (H^+ and H^-) as a function of various spatial and temporal parameters (Halekas, 2017; Henderson et al., 2021, 2022; Jones et al., 2022).

The properties of H^-, in particular, have been left largely unexplored. One previous study examined how these particles' fluxes vary with respect to season, upstream solar wind energy, and how H^- densities compare to upstream solar wind protons and penetrating H^+ (Jones et al., 2022). In this manuscript, we seek to focus on the behaviors of H^- in the Martian atmosphere using a combination of in situ data and mathematical models. We examine data collected by the Mars Atmosphere and Volatile EvolutioN (MAVEN) spacecraft to determine under what conditions H^- is most often observed at Mars (Jakosky et al., 2015). We cross-compare the observed fluxes of H^- and H^+ as a function of atmospheric CO_2 column density. We then use a previous framework outlined in Halekas (2017) describing the evolution of the charge fraction of H^+ as a function of altitude to discuss the anticipated equilibrium behaviors of H^-. We develop a simple model describing the neutral and negative charge fractions of hydrogen ENAs and H^- by examining the effects of charge exchange, electron attachment, and photodetachment. Finally, we compare our modelling results to our data set.

2 H^- In Situ Observations

Before modeling the behavior of H^-, we are interested in characterizing how these particles behave in the Mars atmosphere by utilizing in situ data. We focus on isolating MAVEN observations where H^- and H^+ ions are present. The following sections describe how we obtain the H^- data, as well as under what conditions we most frequently observe this particle population. We also briefly compare how H^- and H^+ fluxes vary with respect to CO_2 column density.

2.1 Methodology

We begin by examining Solar Wind Ion Analyzer (SWIA) and Solar Wind Electron Analyzer (SWEA) L2 archive data collected during MAVEN dayside periapses at altitudes below 250 km between 2014 and 2023 (Halekas et al., 2015; D. Mitchell et al., 2016).

For each orbit, we determine if the Sun is within SWEA's and/or SWIA's field of view (FOV). Due to the position of both instruments on MAVEN in addition to the spacecraft's orbital configuration, the Sun may not necessarily be within the instruments' FOVs during each periapsis (Halekas et al., 2015; D. Mitchell et al., 2016). Depending on the orbital configuration, the Sun may only be observable by one of the instruments. In order to best detect both H^+ and H^-, it is critical that the instruments are pointed sunward since solar wind hydrogen ENAs are highly collimated in the antisunward direction. Once we confirm that the Sun is in the relevant instrument's FOV, we proceed to analyze the electron and ion data collected within that periapsis.

Due to low count statistics, we first determine an average background count rate for each orbit. We separate the electron data into backscattered and downward populations using the same methods described in Girazian and Halekas (2021). Namely, we determine the dot product between the electron's velocity vector and Mars surface normal for a given measurement. If the dot product is positive, this is considered backscattered; the opposite is true for the downward condition (Girazian & Halekas, 2021). Due to SWEA's position on MAVEN, specific anode bins are physically blocked by the spacecraft; we therefore exclude these bins from our analysis within the downward and backscattered data (D. Mitchell et al., 2016). Once these anodes are masked, we compute an angular sum to generate an energy-count profile for a given timestamp and repeat this process for each individual 8-second observation during a periapsis. We also implement an outlier rejection to the SWEA data to better isolate the H^- signal. It has been shown that magnetosheath electrons are able to precipitate into the upper Martian atmosphere under certain magnetic field configurations, resulting in "hot" electron signatures visible below altitudes of 250 km (D. L. Mitchell et al., 2001). To mitigate this, we sum the electron counts for energies above 600 eV in each time bin collected over a periapsis for both the backscattered and downward populations. Once we obtain total counts per time stamp in each direction, we find the median total counts for a given periapsis in each respective direction. Any timestamps where the total counts exceed 2.5 times the periapsis median is rejected. This threshold was chosen empirically after examining a multitude of periapses. We then proceed to sum over all timestamps for the duration of the periapsis for the backscattered data, resulting in an angular-averaged count-energy profile. From this total backscattered profile, we take the average number of counts in the three highest energy bins to generate an average background for a given periapsis.

Once this average background is obtained from the backscattered data, we turn to the downward propagating data. The main purpose of obtaining the background for each periapsis is two-fold: to determine whether the total H^- signal is statistically significant compared to that of the background and to perform a background subtraction. To determine if the H^- signal is significantly different from that of the background (BG), we first isolate the total core counts (C_{core}) that are collected at energies within $0.83E_{SW} \leq E_{SW} \leq 1.34E_{SW}$, where E_{SW} is the upstream solar wind energy for that particular orbit. This range of energies was chosen in order to encompass neighboring energy bins for SWEA, given that the instrument's resolution is 17% (D. Mitchell et al., 2016). We tailor this limit towards higher energies in order to prevent signals from low energy sources (i.e., Auger electrons) from dominating our signal.

We repeat these methods on the SWIA H^+ data with two subtle changes. For the hot population filter, we sum over energies above 200 eV; this range is imposed in order to eliminate potential spacecraft charging signatures while still detecting planetary ion populations or accelerated heavy ions (Halekas et al., 2017). The second change that we implement is the range of energies we examine in order to isolate each distribution's core points. We focus on energy bins that satisfy $0.855E_{SW} \leq E_{SW} \leq 1.29E_{SW}$; these limits were chosen due to SWIA's intrinsic resolution of 14.5% (Halekas et al., 2015).

Once we remove hot populations in both the H^- and H^+ data, we then compare the distribution of isolated core counts to the background counts of each population's signal. To do so, we compute a z-score using a right-tailed Z test,

$$z = \frac{\overline{C_{core}} - \overline{BG}}{\sqrt{(\sigma_{core}/\sqrt{N_{core}})^2 + (\sigma_{BG}/\sqrt{N_{BG}})^2}}, \tag{1}$$

where $\overline{C_{core}}$ is the average of the isolated core points, $\overline{BG}$ is the average of the background counts, σ_{core} is the standard deviation of the core counts, σ_{BG} is the standard deviation of the background counts, N_{core} is the number of core counts, and N_{BG} is the number of background counts. Note that these standard deviations are computed using Bessel's correction to account for bias in small population samples. We ultimately convert these z-scores into a more familiar p-value using a right-tailed test lookup table.

In addition to computing a z-score, we also compute a signal to noise ratio (SNR) for each periapsis. We implement this statistic as well after examining the distribution of p-scores for the H^- signals. To compute a SNR, we compare the core counts to those of the background. We find the peak total number of counts in the core of the distribution and take the ratio of this and the average background counts. After examining various orbits, we determine that a SNR ≥ 3 quantifies a statistically significant signal.

After repeating the above process for H^- and H^+ data, we conclude that further visual confirmation is needed to determine if an H^- signal is actually present. Figure 2 shows the distribution of SNRs and p-scores for the dayside orbits between 2014 and 2023 where data were available for SWEA and/or SWIA. We see a clear difference between

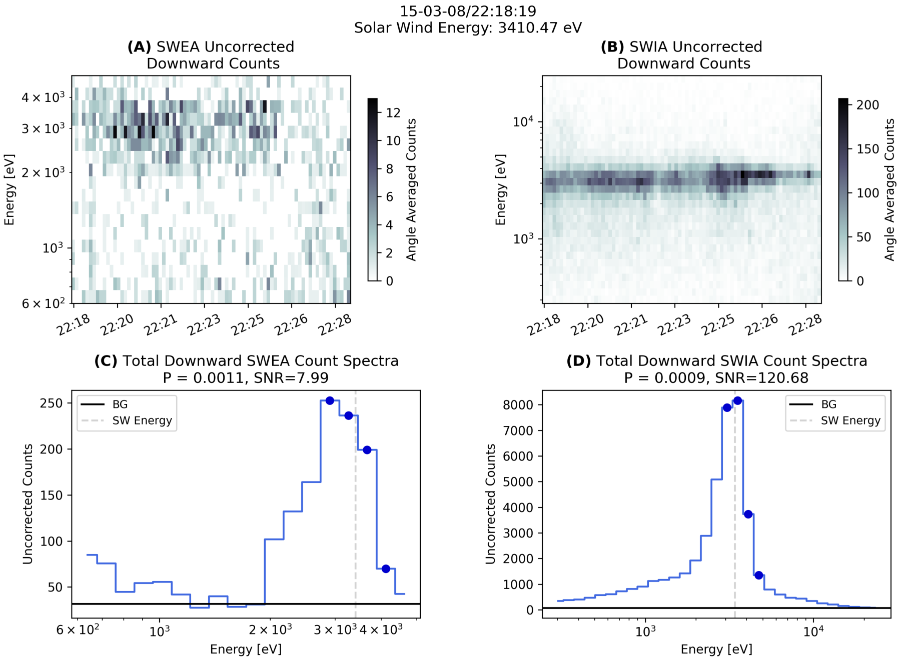

Figure 1. Example of SWEA and SWIA uncorrected count-energy spectra from a coronal mass ejection event on March 8, 2015. (A) Downward, angle summed count profile for SWEA without background correction. (B) Same as Panel A, but for SWIA. (C) Coadded SWEA orbital profile resulting from summing over all timestamps in Panel A. Blue points represent C_{core}. (D) Same as Panel C, but for SWIA. Note different scaling on each subpanel.

the two datasets; SWIA H^+ data are significantly more robust than SWEA H^- data. Of the 2,344 SWEA observations available, 1,708 (72.9%) had background levels that were higher than the core counts. Of SWIA's 4,247 available observations, only 186 (4.38%) demonstrated this behavior. When examining the distribution of orbits that satisfy what we deem as a statistically significant threshold (SNR $\geq$ 3 and p $\leq$ 0.05), we are left with 68 SWEA orbits and 2,761 SWIA orbits. Upon further inspection of numerous orbits, we find that the backscattered signal detected by SWEA in its highest energy bins is sometimes higher than anticipated. This skews the p-score and SNR to values outside of what we would nominally deem statistically significant, even if an H^- signal is indeed present. We also find that during orbits with upstream solar wind energy less than ~1000 eV, the p-score and SNR are often skewed towards more statistically significant values due to high signals of Auger electrons contaminating the region where we anticipate H^- to be present. Because of these factors, we examine all available orbits by eye to determine if a signal is detected, an example of which can be seen in Figure 1. Once we visually confirm that an H^- signal is present within a given periapsis, we proceed to analyze each 8-second or 4-second slice of downward propagating H^- and H^+ data, respectively.

We compute an average background count rate for a given periapsis by dividing $\overline{BG}$ by the duration of the periapsis in seconds. We then apply a background correction to each energy-anode bin using this background count rate to try and eliminate instrument background and counts generated by high energy particles, such as cosmic rays. After applying this correction, we convert these background corrected counts into differential energy flux. We then sum over all anode bins to generate an angular-averaged profile for the downward population observed during each individual timestamp. This

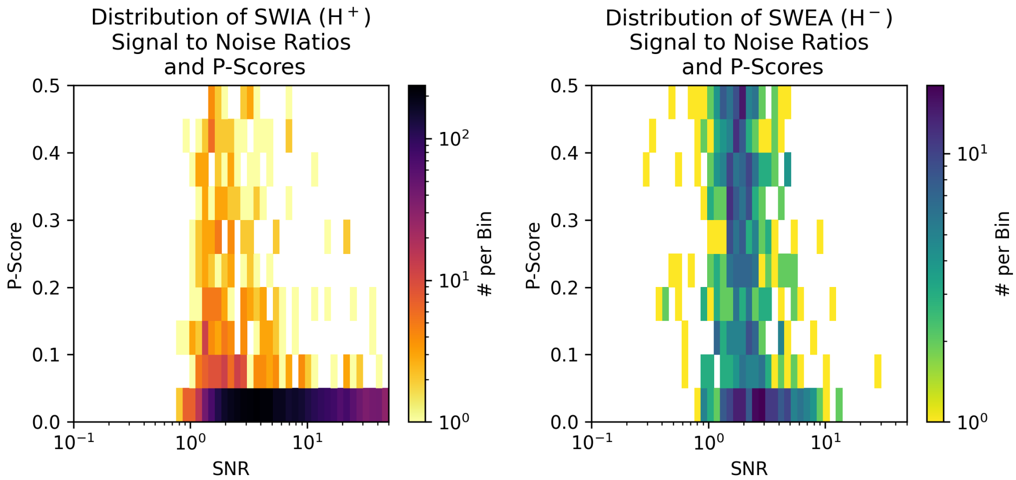

Figure 2. Distribution of p-scores and signal to noise ratios (SNRs) for SWIA and SWEA dayside periapses between 2014 and 2023. Note different scaling on colorbars.

process is repeated for both SWEA and SWIA data at an 8-second or 4-second cadence, respectively.

With the aforementioned energy restrictions, FOV constraints, L2 archive data availability, and visual confirmation, we are only left with 43 periapses to cross compare H^+ and H^-.

2.2 Results

We seek to compare the behavior of H^+ and H^- in the Martian atmosphere by examining temporal and spatial characteristics of their energy spectra. As is apparent from Figure 1, the flux of H^- is significantly lower than that of H^+ and other ion species within the Martian ionosphere. Particularly, the backscattered signal of H^- is extremely diminished; we therefore only examine downward propagating populations of H^+ and H^- in this analysis.

2.2.1 Distribution of H^- Detections

Since detection of H^- events is rare (1.8% of available orbits), we first want to determine under what conditions these particles are most frequently observed. Figure 3 summarizes the distribution of these orbits as a function of various relevant parameters.

We see a clear bias towards H^- events occurring near perihelion (L_S=251°) and during southern summer (270° $\leq L_S \leq$ 360°). This is not surprising, given the seasonal increase in the exposed hydrogen column density upstream of the Martian bow shock, which allows for an increased rate of ENA generation and consequent charge-changing processes (Halekas, 2017). Additionally, dust season occurs within southern summer; dust storms have been shown to sweep up water molecules to ionospheric altitudes, where they can undergo photodissociation (Chaffin et al., 2021). This process creates a larger source of hydrogen within the upper atmosphere of Mars, which may also aid in the creation of more H^- ions. In conjunction with a seasonal bias, we also observe a higher occurrence of H^- precipitation events for high solar wind energies. We would also anticipate this trend for two reasons: an increased cross section of interaction and easier discern-

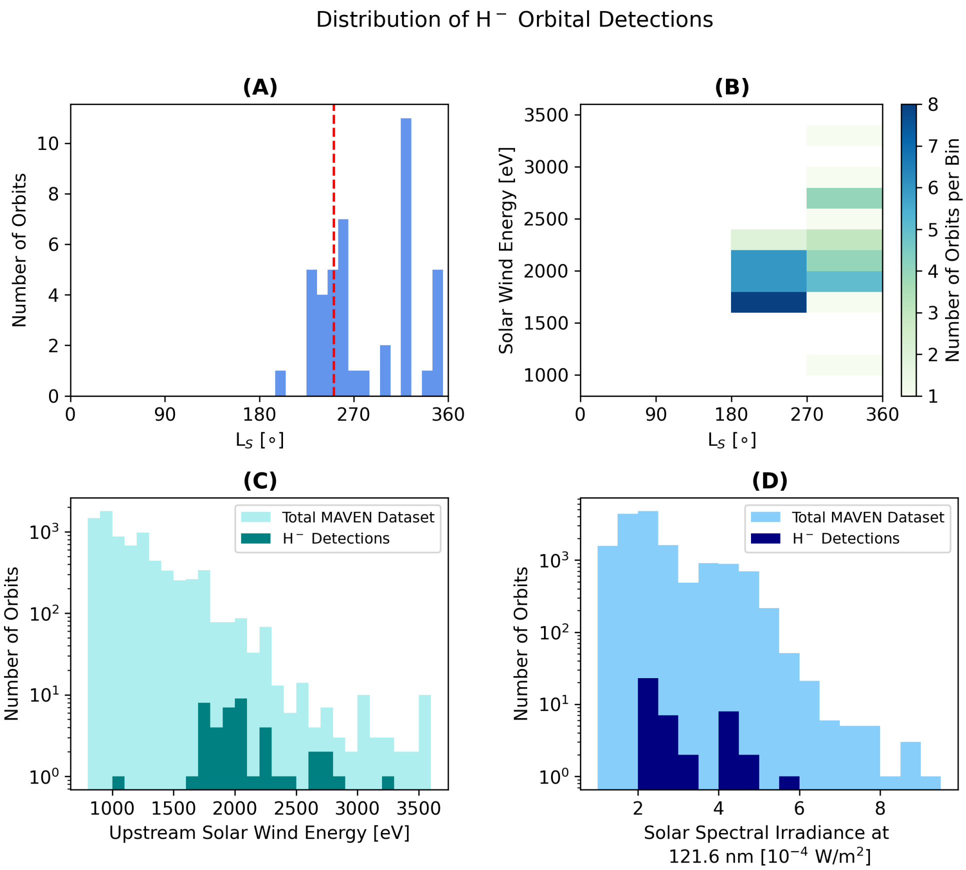

Figure 3. Distribution of orbits with H^- detections with respect to solar longitude (L_S), solar wind energy, and solar EUV irradiance. Red vertical line in Panel A indicates perihelion ($L_S = 251°$).

ment from other electron populations at Mars. The cross section for electron attachment increases significantly with increasing solar wind energy (Lindsay et al., 2005). Additionally, Auger and/or photoelectrons are not present at these higher energies, which also allows us to see H^- precipitation much more clearly.

Another potentially important factor affecting H^- precipitation is solar extreme ultraviolet (EUV) emission. Utilizing orbit-averaged L2 data from the Extreme Ultraviolet Monitor (EUVM) onboard MAVEN, we examine the distribution of H^- events as a function of solar Lyman-α emission (Eparvier et al., 2015). In Figure 3 Panels B and D, we do not see any strong correlation between H^- precipitation and solar EUV irradiance. Compared to the overall distribution of solar EUV irradiance measurements collected over the duration of the MAVEN mission, we do not see any particular bias in H^- detections towards high or low periods of solar flux. This indicates that H^- precipitation should occur throughout various points of the solar cycle, which is indeed what we observe in Figure 4.

From Figure 4A, we see that the majority of H^- detections are clustered in 2016 near perihelion during the declining phase of Solar Cycle 24. We also observe a second cluster of events in 2022 as we approach Solar Cycle 25 maximum, where the solar EUV input is $\sim$2-3 times larger than during solar minimum. This distribution of events indicates that there is no strong correlation between solar cycle and observed H^- precipitation. Figure 4B summarizes the distribution of events as a function of solar EUV irradiance as well as solar wind energy. We see from this panel that events occurring during periods of lower EUV input are observed at a broader range of energies when compared to those that occur near solar maximum.

We also see in Figure 4A that all events prior to 2022 are primarily clustered near perihelion. This can most likely be attributed to the seasonal variability of the hydrogen corona; at perihelion, the exposed hydrogen column density upstream of the bow shock increases by a factor of $\sim$3 compared to aphelion (Halekas, 2017). Having more hydrogen available upstream of the bow shock allows for a higher production rate of ENAs (up to $\sim$5%), which ultimately allows for a higher likelihood of H^- and H^+ precipitation (Halekas, 2017).

The trends presented in Figures 3 and 4 seem to indicate that there is a "sweet-spot" for H^- precipitation in the upper atmosphere of Mars. We observe a bias in H^- precipitation events during high energy solar wind conditions, which often coincide with heightened periods of solar activity. We also observe most precipitation events near perihelion, where both the solar EUV irradiance and the amount of exposed hydrogen column density upstream of Mars's bow shock peak in the planet's orbit about the Sun. Shortly after perihelion, we observe an uptick in H^- precipitation events during southern summer solstice, which coincides with Mars's dust season. We also observe precipitation events at various points within the solar cycle, suggesting there is not a strong dependence of H^- precipitation on solar EUV emission. With all of these factors, it appears that there are a multitude of drivers that affect H^- precipitation. Our findings suggest a delicate balance between solar wind conditions, solar activity, and Martian atmospheric conditions is required in order to observe H^-. Further observations are required to better understand the behaviors presented here.

2.2.2 Column Density Variation

In addition to examining the distribution of H^- precipitation events, we also want to investigate the behavior of H^- and H^+ congruently as a function of atmospheric CO_2 column density. Using CO_2 data from the Neutral Gas and Ion Mass Spectrometer (NGIMS), we compute column density values for each 8-second SWEA and 4-second SWIA measurement within our 43 orbit sample (P. Mahaffy et al., 2015). To obtain each column density value, we trace the path of the precipitating solar wind hydrogen from the Sun

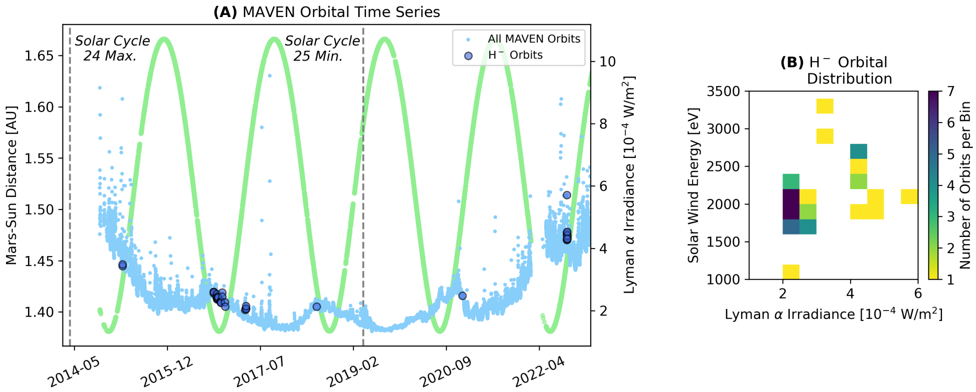

Figure 4. (A) Time series of orbit-averaged solar EUV irradiance from MAVEN Extreme Ultraviolet Monitor (EUVM) observations. Light blue points represent all orbit-averaged solar EUV irradiances, while dark blue points represent orbits where H^- was detected. Green points show the Mars-Sun distance in astronomical units, with the corresponding axis on the left-hand side of the figure. Solar cycle phases are indicated by the text and gray hashed lines. (B) Distribution of H^- orbits as a function of upstream solar wind energy and solar EUV irradiance. Note: The gap in data near April 2022 is due to MAVEN going into safe-mode.

to the point at which it is observed by MAVEN. Ultimately, this quantifies the amount of CO_2 that a given particle has passed through along its path of propagation. The exact details of this calculation are described in Henderson et al. (2021).

Previous studies have demonstrated that H^+ flux varies as a function of column density, increasing as hydrogen ENAs interact with more CO_2 molecules along their path of propagation. This behavior is exhibited up until a critical column density, where H^+ and H production reach an equilibrium; ultimately, a “turnover” in the flux profile is observed where collisional processes and consequential energy loss dominate (Halekas, 2017; Henderson et al., 2021). We anticipate a similar behavior demonstrated by H^-; however, the point at which this turnover occurs may vary due to different physical processes that result in the production/destruction of H^-. To investigate whether these behaviors are present within our H^- observations, we start by examining the average flux profiles of H^+ and H^- using all available orbital data.

Figure 5 summarizes the average behavior of precipitating H^+ and H^- fluxes as a function of CO_2 column density. We see in Panel A that H^+ fluxes increase steadily until $\sim 6\times10^{14}$ cm^{-2}, at which point they seemingly plateau. At 5.25×10^{15} cm^{-2}, we note a slight increase in the flux relative to this plateau and also see a dramatic falloff in the flux profile thereafter, decreasing by a factor of $\sim$4. We do not observe such stark behavior in Panel B. The H^- fluxes do not increase as rapidly with respect to column density as H^+. We note, however, that the H^- fluxes begin to plateau at $\sim 3\times10^{14}$ cm^{-2} and experience a smooth decline starting at 10^{16} cm^{-2}.

We see from Panels A and B that H^+ is much more favorably created through charge exchange than H^-, as indicated by nearly an order of magnitude difference in the average peak fluxes. This is reflected in Panel C, where we observe a peak flux ratio of $\sim$8. Across the entire range of column densities, H^+ flux is $\sim$4.5 times greater than that of H^-. Clearly, ENAs are preferentially converted to H^+ along their path of propagation;

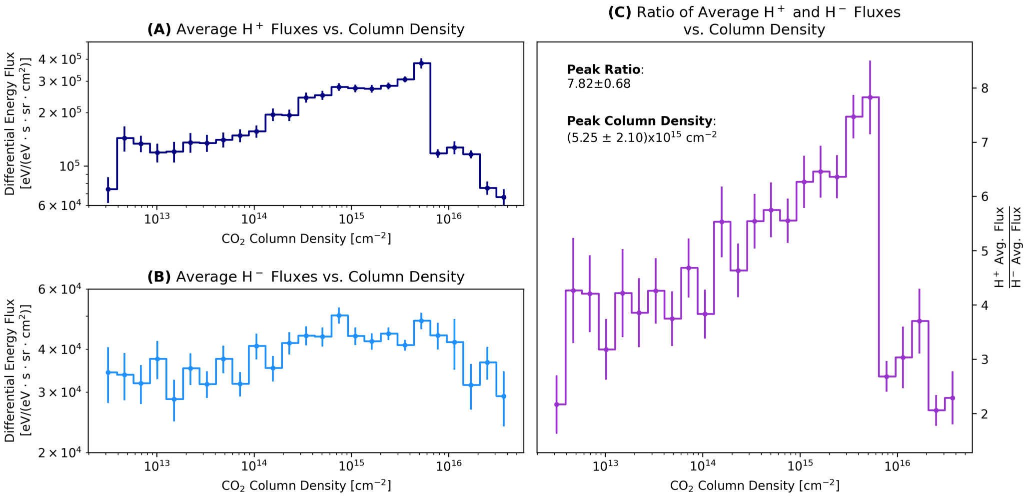

Figure 5. Average profiles of H^+ and H^- fluxes from 43 periapses. (A) Behavior of H^+ flux as a function of CO_2 column density. Mean is taken per column density bin, with the standard error of the mean shown as error bars. (B) Same as Panel A, but for H^-. Note different scaling. (C) Ratio of average H^+ and H^- fluxes versus CO_2 column density.

this is not surprising, given the magnitude of the cross sections for electron stripping versus electron attachment (Lindsay et al., 2005).

3 H^- Mathematical Model

Previously, Halekas (2017) constructed a simple model for charge equilibrium between H and H^+ by implementing cross sections for interactions between these two particle species and CO_2. They described the evolution of the charged (F^+) and neutral (F^0) fractions of these populations, respectively, as a function of altitude using a coupled set of differential equations. Utilizing the same framework, we can repeat this analysis for H^-.

When discussing the behavior of H^- in the atmosphere of Mars, we must consider three primary processes: electron attachment ($H + CO_2 \rightarrow H^- + CO_2^+$), charge exchange ($H^- + CO_2 \rightarrow H + CO_2^-$), and photodetachment ($H^- + \gamma \rightarrow H + e^-$). To most accurately represent the behavior of precipitating ENAs, one should compute a weighted sum over all of the various particle species that these hydrogen ENAs collide with in the upper atmosphere. However, for altitudes below 250 km, CO_2 comprises over $\sim$95% of the Martian atmosphere; thus, it is a reasonable first-order approximation that CO_2 is the dominant species with which ENAs and their charged byproducts can interact (Nier & McElroy, 1977; P. R. Mahaffy et al., 2015).

Following the framework of Halekas (2017), we can construct a coupled set of equations describing the evolution of ENAs and H^- as we progress through the Martian atmosphere. Accounting for charge exchange, electron attachment, and photodetachment, we arrive at the following,

$$\frac{dF^-}{dr} = [\sigma_{02}(E)F^0(r) - \sigma_{20}(E)F^-(r)]n_{CO_2}(r) - N_{PD}(r,E)F^-(r) \tag{2}$$

$$\frac{dF^0}{dr} = [\sigma_{20}(E)F^-(r) - \sigma_{02}(E)F^0(r)]n_{CO_2}(r) + N_{PD}(r,E)F^-(r), \tag{3}$$

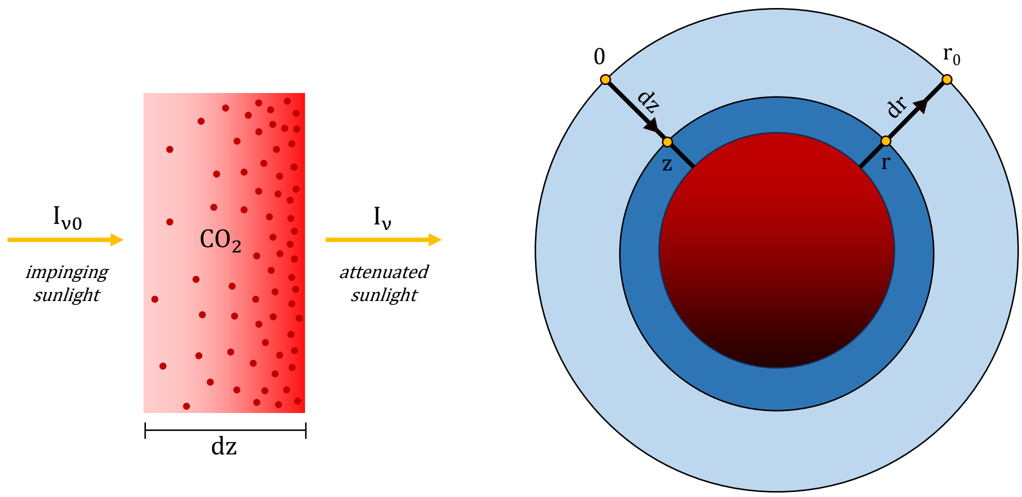

Figure 6. Outline of set up for photodetachment calculation. Left figure shows sunlight ($I_{\nu 0}$) hitting CO_2 slab. Attenuated light (I_ν) displayed on right side of slab. Right figure outlines the coordinates implemented in this calculation, with Mars at the center in burgundy. Yellow points show location of integration limits.

where F^- is the fraction of precipitating hydrogen ENAs converted to H^-, F^0 is the fraction of H^- converted to ENAs, n_{CO_2} is the CO_2 number density, r is altitude, σ_{02} is the cross section for electron attachment of H by CO_2, σ_{20} is the cross section for charge exchange of H^- with CO_2, and N_{PD} represents the number of photodetachments over a unit distance. We do not include the effects of H^+ charge exchange with CO_2 in this system, which can alter F^0 by 4 - 15% (Halekas, 2017); this is left for future examination. The charge exchange and electron attachment terms within Equations 2 and 3 are well characterized; however, we need to derive the photodetachment term, N_{PD}.

3.1 Photodetachment Term Derivation

To determine the number of interactions an impinging particle experiences over a given time, we can write the following expression,

$$k = n\sigma v, \tag{4}$$

where n is the number density of the target particle species, σ is the cross section of the given interaction, and v is the velocity of the impinging particle. This can be easily rewritten as an interaction rate per unit length if we simply divide Equation 4 by the incoming particle's velocity, v. Examining the first two terms on the right-hand side of Equations 2 and 3, we can see that the units of these terms are congruent with k/v. Therefore, we can determine the rate of photodetachment and divide this by the velocity of H^- in order to determine the number of photodetachments that occur over a given unit length (N_{PD}).

To do this, we first need to determine how solar light is attenuated by the CO_2 dominated Martian atmosphere. This will help us to characterize the rate of photodetachment as a function of altitude as CO_2 density varies. Assuming we have sunlight impinging on a slab of CO_2, we can write a basic set of equations describing how the flux of solar photons varies with respect to the thickness of the CO_2 slab (or rather, altitude). Figure 6 outlines the set up of this problem.

From basic radiative processes, we can write the following,

$$\frac{dI_\nu(\nu,z)}{dz} = -n_{CO_2}(z)\sigma(\nu)I_\nu(\nu,z), \tag{5}$$

where I_ν is the specific intensity of light, dz is the thickness of the CO_2 slab, n_{CO_2} is the number density, ν is the frequency of light, and σ is the cross section of a given interaction between the incoming photons and CO_2. In principle, the cross section term should encompass all possible chemical processes, including collisional excitation, absorption, and emission. However, we only include photoabsorption (σ_{PA}) by CO_2 to simplify our model.

Integrating Equation 5 using the limits described in Figure 6, we arrive at the following,

$$\int \frac{dI_\nu(\nu,r)}{I_\nu(\nu,r)} = -\int_r^{r_0} \sigma_{PA}(\nu)n_{CO_2}(r')\ dr'. \tag{6}$$

We can define an expression for atmospheric column density,

$$N_{COL} \equiv \int_r^{r_0} n_{CO_2}(r')\, dr.' \tag{7}$$

Utilizing this definition, the integral on the right-hand side of Equation 6 can simply be expressed as a function of column density,

$$\int \frac{dI_\nu(\nu,r)}{I_\nu(\nu,r)} = -\sigma_{PA}(\nu)N_{COL}. \tag{8}$$

Evaluating Equation 8 leads to a solution for I_ν,

$$I_\nu(\nu, N_{COL}) = I_{\nu 0}(\nu)e^{-\sigma_{PA}(\nu)N_{COL}}, \tag{9}$$

where $I_{\nu 0}(\nu)$ is the solar specific intensity at the top of the Martian atmosphere. Solar specific intensity is conserved as a function of distance and is well described by the Planck function for a blackbody emitting at T = 5,800 K. Naturally, the solar spectrum is not a perfect blackbody, as has been shown by previous studies (Huebner et al., 1992; Huebner & Mukherjee, 2015). However, we utilize this assumption in our calculation to simplify our mathematical model. With all of these moving parts and substituting for energy, we can finally write I_E as a function of photon energy, blackbody temperature, and column density,

$$I_E(E,T,N_{COL}) = \left(\frac{2E^3}{c^2h^2}\frac{1}{e^{E/kT}-1}\right)e^{-\sigma_{PA}(E)N_{COL}}. \tag{10}$$

As previously mentioned, we seek to quantify the photodetachment rate at a given point within the Martian atmosphere in order to characterize the fraction of H^- converted to H due to photodetachment. Now that we have determined how solar radiation is attenuated by CO_2, we can proceed to calculate the photodetachment rate.

The photodetachment rate can be written in the following way,

$$k = \int_{\Omega_0}^{\Omega_f} d\Omega \int_{E_0}^{\infty} \frac{I_E(E,T,N_{COL})}{E\cdot h}\sigma_{PD}(E)dE, \tag{11}$$

where Ω is the solid angle, and σ_{PD} is the photodetachment cross section (McLaughlin et al., 2017). Substituting Equation 10 into 11, we arrive at the following,

$$k = \int_{\Omega_0}^{\Omega_f} d\Omega \int_{E_0}^{\infty} \sigma_{PD}(E)\left(\frac{2E^2}{c^2h^3}\frac{1}{e^{E/kT}-1}\right)e^{-\sigma_{PA}(E)N_{COL}}dE. \tag{12}$$

Using simple geometry, we can write the total solid angle through which the solar radiation passes,

$$\Omega = 4\theta cos(\pi/2 - \theta), \tag{13}$$

where $\theta = \arctan(R_\odot/d_{MS})$, $R_\odot$ is the radius of the Sun, and d_{MS} is Mars-Sun distance. If we evaluate Equation 13 using Mars-Sun distances for aphelion and perihelion, we obtain $\Omega = [3.1112 \cdot 10^{-5}\ , 4.5221 \cdot 10^{-5}]$ steradians, respectively.

Combining Equations 12 and 13, we arrive at our final solution describing the rate of photodetachment at a given CO_2 column density in the Martian atmosphere,

$$k = 4\theta cos(\pi/2 - \theta) \int_{E_0}^{\infty} \sigma_{PD}(E) \left(\frac{2E^2}{c^2 h^3} \frac{1}{e^{E/kT} - 1} \right) e^{-\sigma_{PA}(E) N_{COL}} dE. \tag{14}$$

We can see from Equation 14 that there are still two undefined parameters: $\sigma_{PD}(E)$ and $\sigma_{PA}(E)$. These variables quantify photodetachment and photoabsorption cross sections, respectively, and do not have analytical forms. We therefore implement measured values of these parameters across various photon energies to obtain a numerical solution for k (Chandrasekhar, 1945; Branscomb & Smith, 1955; Sun & Weissler, 1955; Smith & Burch, 1959; Cairns & Samson, 1965; Conrath et al., 1973; Wishart, 1979; Craver, 1982; Lewis & Carver, 1983; Rahman & Hird, 1986; Yoshino et al., 1996; Parkinson et al., 2003; Stark et al., 2007; McLaughlin et al., 2017).

One aspect to note is the temperature dependence of the photoabsorption cross sections utilized in this study. As we progress through the Martian atmosphere, the temperature profile varies. In the case of CO_2 in the range of altitudes we examine, the temperature varies from approximately 180 K to 245 K (Stone et al., 2018). The photoabsorption cross sections utilized in our calculations were obtained at a temperature of 195 K; thus, our photodetachment rate will be an approximation based on the assumption that CO_2 photoabsorption cross sections do not vary significantly with temperature.

We can determine k by implementing the various measured cross sections for photodetachment and photoabsorption. To do so, we integrate Equation 12 over energies where photodetachment cross sections are nonzero. From Supplemental Figure S1, we see that the relevant energy ranges fall between the near infrared and EUV. Previous measurements have demonstrated that Martian atmospheric transmittance of solar photons is most impeded by CO_2 in the infrared at wavelengths between $\sim$2 and 13 μm (Conrath et al., 1973). If we examine Supplemental Figure S1, we find that these near infrared wavelengths are outside the domain where photodetachment is prevalant. The infrared photoabsorption cross sections are therefore irrelevant, since the photodetachment cross section tends towards zero in this frequency range. We do note, however, that there is an overlap in photoabsorption and photodetachment in the EUV regime and proceed to evaluate Equation 14 over this frequency range.

Integrating Equation 14 over energies $\sim 10^{-1} - 10^5$ eV, we obtain a photodetachment rate that depends only on Mars-Sun distance. Upon evaluating Equation 14 for column densities $10^9 - 10^{18}$ cm^{-2} for a given Mars-Sun distance, we observe a (9.25×10^{-6})% change in the photodetachment rate between the maximum and minimum column density. This indicates that attenuation due to CO_2 photoabsorption is negligible, and thus the column density dependence in Equation 14 can be neglected.

With these results, we can further simplify Equation 14. If we set the photoabsorption term $(e^{-\sigma_{PA}(E)N_{COL}})$ to unity and integrate over all EUV energies, our integrand simplifies to 2.0244×10^5 s^{-1} sr^{-1}. We can now express the rate of photodetachment in the following manner,

$$k = (2.0244 \times 10^5) \left[4\theta cos(\pi/2 - \theta)\right]. \tag{15}$$

Evaluating the above equation during aphelion and perihelion results in photodetachment rates of $\sim$6 and $\sim$9 per second, respectively. This is in relatively good agreement with photodetachment rates obtained in previous studies using measured solar photon flux at 1 AU (Huebner et al., 1992; Desai et al., 2021). Extrapolating the results from these studies to Mars (i.e., 1.3814 - 1.666 AU) results in rates between ∼5 and ∼7 photodetachments per second, which is congruent with our derivation.

If we recall Equation 4, we can now write $N_{PD} = k/v_{H^-} = k\sqrt{m_{H^-}/2E}$, where m_{H^-} is the mass of H^-. This allows us to write a full expression describing the behavior of hydrogen ENAs and H^- as they interact with both solar photons and the Martian atmosphere:

$$\frac{dF^-}{dr} = [\sigma_{02}(E)F^0(r) - \sigma_{20}(E)F^-(r)]n_{CO_2}(r) - (2.0244 \times 10^5)\,[4\theta cos(\pi/2-\theta)]\sqrt{\frac{m_{H^-}}{2E}}F^-(r) \quad (16)$$

$$\frac{dF^0}{dr} = [\sigma_{20}(E)F^-(r) - \sigma_{02}(E)F^0(r)]n_{CO_2}(r) + (2.0244 \times 10^5)\,[4\theta cos(\pi/2-\theta)]\sqrt{\frac{m_{H^-}}{2E}}F^-(r). \quad (17)$$

3.2 Numerical and Analytical Solutions

Before explicitly solving Equations 16 and 17, we can examine how the number of interactions per unit length for electron attachment, charge exchange, and photodetachment varies with respect to CO_2 atmospheric density by quantifying each coefficient within these coupled differential equations. Utilizing the cross sections for electron attachment and charge exchange collected between 1 and 3 keV, we can calculate the quantity of each coefficient within Equations 16 and 17 and determine at which point within the Martian atmosphere a given process dominates (Nakai et al., 1987; Lindsay et al., 2005). Figure 7 summarizes how these three processes vary with respect to altitude using this approach.

It is important to note that the cross section for charge exchange between H^- and CO_2 has not been measured within the energy range we examine here. Previous studies have utilized O_2 cross sections to generate proxy cross sections for CO_2 when measurements were not available (Kallio & Barabash, 2000, 2001). We employ this method in our analysis as well.

Nakai et al. (1987) measured the cross section of charge exchange between H^- and O_2 for energies spanning 1 eV to 10 MeV. They also measured the cross section of charge exchange between H^- and CO_2 (σ_{20} in our analysis), but only at energies greater than 20 keV. In order to extrapolate σ_{20} to solar wind energies, we employ a scaling factor. We average the ratio of the O_2 cross section to the CO_2 cross section in the 20 keV to 10 MeV range. We then multiply the entire O_2 cross section profile by this average ratio to obtain proxy values of σ_{20} at energies pertinent for our analysis here (Nakai et al., 1987).

We observe a few interesting behaviors in Figure 7. First and foremost, we see in Panels A and B that charge exchange is the primary process governing H^- for altitudes below 194 ± 5 km across various energies and Mars-Sun distances. Above this threshold, however, we note that photodetachment overtakes both electron attachment and charge exchange processes. Further examination of Panel A indicates that the altitude range at which electron attachment overtakes photodetachment is much lower than that of charge exchange. Panel B shows that photodetachment remains significantly important compared to electron attachment at altitudes above 134 ± 8 km. This feature becomes most important at perihelion for low energy solar wind conditions. Figure 7 indicates that photodetachment becomes relatively negligible at ionospheric altitudes below ∼125 km. However, in the upper ionosphere, it appears that this H^- sink cannot be ignored.

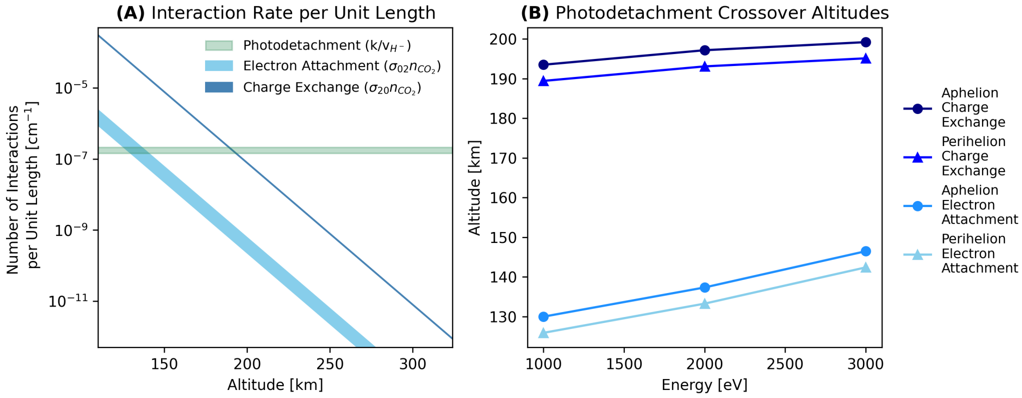

Figure 7. Summary of interactions per unit length for charge exchange, electron attachment, and photodetachment. (A) The upper bound for electron attachment was determined using cross sections at 3 keV, while the lower bound was determined using 1 keV cross sections. The inverse of this applies to the charge exchange curve. The upper bound of the photodetachment curve represents the value at perihelion for $E_{H^-} = 1$ keV, while the lower bound is at aphelion. The altitude values and corresponding density values were calculated using the average CO_2 profile from Supplemental Figure S2. (B) Summary of altitudes at which photodetachment becomes dominated by either charge exchange or electron attachment (i.e., where the blue regions overlap the green region in Panel A). Curves are separated by Mars-Sun distance and relevant process, as indicated in legend.

3.2.1 Analytical Solution Derivation

For altitudes below 125 km, we can find an approximate solution to Equations 16 and 17 by assuming k $\rightarrow$ 0. This leaves us with differential equations in the following form,

$$\frac{dF^-}{dr} = [\sigma_{02}F^0(r) - \sigma_{20}F^-(r)]n_{CO_2}(r) \tag{18}$$
$$\frac{dF^0}{dr} = [\sigma_{10}F^-(r) - \sigma_{01}F^0(r)]n_{CO_2}(r). \tag{19}$$

If we add Equations 18 and 19, we find that $\frac{dF^-}{dr} = -\frac{dF^0}{dr}$. This, combined with the boundary conditions of $F^-(\infty) = 0$ and $F^0(\infty) = 1$, results in

$$F^0(r) = 1 - F^-(r). \tag{20}$$

We can write the density in Equations 18 and 19 analytically if we assume that the atmosphere is in equilibrium. This is true for altitudes below 300 km in the Martian atmosphere, which is approximately the upper limit of the altitudes we examine here (Cravens et al., 2017). We can write the CO_2 density profile in an exponential form,

$$n_{CO_2}(r) = N_0 e^{mr}, \tag{21}$$

where N_0 is a reference CO_2 number density, and the magnitude of m is the inverse of the atmospheric scale height. Substituting Equations 20 and 21 into Equation 18, we are left with a differential equation in the following form:

$$\frac{dF^-}{dr} + (\sigma_{02} + \sigma_{20})N_0 e^{mr} - \sigma_{02}N_0 e^{mr} = 0. \tag{22}$$

Equation 22 has a solution for the negative charge fraction,

$$F^{-}(r) = \frac{\sigma_{02}}{\sigma_{02} + \sigma_{20}} \left[1 - e^{\frac{-N_0(\sigma_{02}+\sigma_{20})}{m} e^{mr}}\right]. \tag{23}$$

Recalling Equation 7, we can rewrite the argument of the exponent in Equation 23 as a function of CO_2 column density. Substituting Equation 7 into Equation 23 and utilizing Equation 20 to solve for $F^0(r)$, we arrive at approximate analytic solutions for the negative and neutral fractions,

$$F^{-}(r) = \frac{\sigma_{02}}{\sigma_{02} + \sigma_{20}} \left[1 - e^{-(\sigma_{02}+\sigma_{20})N_{COL}}\right] \tag{24}$$

$$F^{0}(r) = \frac{\sigma_{20}}{\sigma_{02} + \sigma_{20}} \left[1 + \frac{\sigma_{02}}{\sigma_{20}} e^{-(\sigma_{02}+\sigma_{20})N_{COL}}\right]. \tag{25}$$

If we assume that precipitating solar wind hydrogen atoms reach approximate equilibrium after one e-folding scale, we can determine from Equations 24 and 25 the equilibrium charge fraction, neutral fraction, and column density. Utilizing this assumption, we arrive at an equilibrium column density,

$$CD_{eq} = \frac{1}{\sigma_{02} + \sigma_{20}}. \tag{26}$$

The negative and neutral fractions converge over ∼5 e-folding scales to a final value expressed by the following equations,

$$F_f^{-} \simeq \frac{\sigma_{02}}{\sigma_{02} + \sigma_{20}} \tag{27}$$

$$F_f^{0} \simeq \frac{\sigma_{20}}{\sigma_{02} + \sigma_{20}}. \tag{28}$$

The electron stripping and charge exchange cross sections vary with respect to the energy of the incoming particle; thus, depending on upstream solar wind conditions, we would anticipate precipitating solar wind hydrogen to reach equilibrium at different column densities within the Martian atmosphere. Using NGIMS CO_2 data, we can explicitly obtain the fit parameters in Equation 21 that describe the average CO_2 density profile as a function of altitude to accurately evaluate Equations 24 and 25. The results of this fitting procedure on inbound verified CO_2 data can be seen in Supplemental Figure S2. These fit parameters, N_0 and m, are then implemented in our column density calculation.

3.2.2 Analytical and Numerical Solution Comparison

As we progress through the atmosphere, we expect the solutions to Equations 16 and 17 to converge to Equations 24 and 25, respectively. However, to understand the role that photodetachment plays at altitudes above 125 km, we can find precise solutions to Equations 16 and 17 across various solar wind energies and Mars-Sun distances using numerical integration methods[1]

Examining the numerical solution for F^- in Figure 8, we find that the maximum charge fraction is 0.78% for high energy solar wind conditions. For lower energy solar wind conditions, this decreases to 0.29%. Kallio et al. (1997) demonstrated that 1-3%

[1] These equations were solved using NDSolve in Mathematica with altitude bounds of 100 - 500 km. The boundary conditions were approximated at an altitude of 500 km. The values of N_0 and m implemented in these calculations can be found in Supplemental Figure S2.

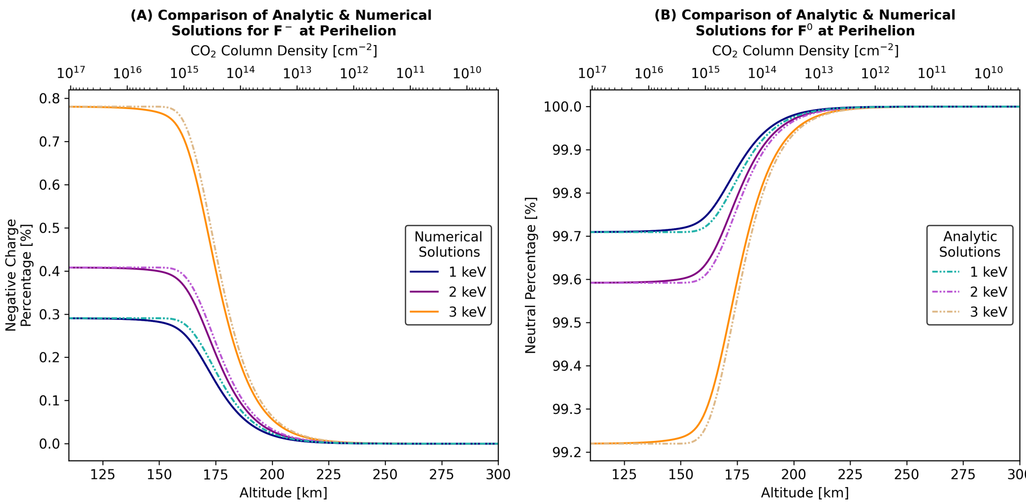

Figure 8. Summary of numerical and analytical solutions for F^- and F^0 at perihelion. Numerical solutions (solid) are obtained from Equations 16 and 17. Analytic solutions (dashed-dotted) are obtained from Equations 24 and 25.

of solar wind protons are converted to ENAs for the energy range we examine here. Combining this with the observed charge fractions determined from our model, this implies that we would anticipate observing 0.0029 - 0.023% of the upstream solar wind proton flux in the form of H^- ions.

Figure 8 summarizes the numerical and analytical solutions across various solar wind energies at perihelion for F^- and F^0. We only examine the results at perihelion since the numerical model does not change significantly as a function of Mars-Sun distance (see Supplemental Figure S3). We see in both panels that there is a slight divergence between the numerical and analytical solutions at altitudes between 130 and 200 km. We find that the fraction of ENAs converted to H^- is slightly lower in the numerical model compared to the analytical model, suggesting that photodetachment is playing a role in depleting the H^- population. If we examine these plots more carefully, we find that the maximum percent difference between the numerical and analytical charge fractions is 1 - 7%. For typical solar wind fluxes ($\sim 10^8$ cm^{-2} s^{-1}), we would anticipate a flux of H^- on the order of $\sim 10^3$ - 10^4 cm^{-2} s^{-1}. In order to detect the effects of photodetachment, we would need to be able to measure fluctuations of ~ 10 - 10^3 cm^{-2} s^{-1}. With SWEA's sensitivity, we would not be able to observe these differences; higher flux H^- events would be required to detect any deviations.

In general, H^- is not preferentially generated in the Martian environment due to the fact that it is so energetically unfavorable. We find that photodetachment dominates the H-H^- system in the upper ionosphere, while atmospheric collisional processes primarily govern these particles below 200 km. We observe a slight difference between our modeling results when photodetachment is included versus when it is excluded. We see a minute increase in the ENAs generated from this process. In practice, this difference would be extremely difficult to observe given our current instrumentation. Only during high energy solar wind conditions would we potentially be able to see the changes in the negative charge fraction induced by photodetachment.

4 Data-Model Comparison

We can now directly compare our observational results from Section 2 to our modeling results from Section 3. Below we will discuss how various aspects of our mathematical model compare to the MAVEN observations previously discussed.

We find that there is not a clear difference in the observed charge fractions as a function of Mars-Sun distance as shown in Supplemental Figure S3, indicating that H^- should be observed throughout various points within the Martian orbit. Figures 3 and 4 indicate that H^- is, however, preferentially observed near perihelion. This is not necessarily contradictory of our model; we do not incorporate variable conditions within the hydrogen corona or lower atmosphere in our framework. Previous studies have found that there is a clear seasonal (and consequently, Mars-Sun distance) dependence on the observed ENA and H^+ flux due to a factor of 3 increase in the exposed hydrogen column density (Halekas et al., 2015; Halekas, 2017). This expansion of the corona creates a larger deposition of ENAs, increasing the likelihood of conversion to H^+ and H^- within the CO_2 atmosphere. It has also been shown that the Martian atmosphere heats and consequently expands during southern summer, affecting hydrogen deposition and CO_2 densities (Halekas et al., 2015; Halekas, 2017; Hughes et al., 2019). These factors would also affect our numerical solutions, shifting them to higher altitudes at perihelion versus aphelion.

Revisiting the trends presented in Figure 4, we observe H^- precipitation at various points within the solar cycle. In principle, we would expect solar EUV emission to affect our observations due to the influence of photodetachment. However, Figure 8 demonstrates the charge fraction is only slightly influenced by this process at altitudes below 200 km. Figure 8 clearly shows that the primary factor at play is the upstream solar wind energy, which greatly impacts the observed charge fraction. Figure 3 bolsters this fact, showing that H^- events are distributed across various solar conditions but occur most often during high energy solar wind conditions.

Additionally, we can directly compare observed number fluxes of the upstream solar wind with those of downstream H^- to determine if the limiting charge fractions that we found in our model align well with observations. We implement the solar wind proxy data for each of our 43 orbits and determine the number flux using the given parameters. In order to compute the density of H^- and H^+ for a given measurement, we utilize the downward, background-corrected differential energy fluxes that we compute in Section 2.1. We then implement Equation 29 for each available measurement,

$$n = \sqrt{\frac{m}{2}}\Delta\Omega \sum_{i=1}^{n} E_i^{-3/2} \Delta E_i F(E_i), \tag{29}$$

where m is the mass of hydrogen, $\Delta\Omega$ is the solid angle, ΔE is the energy channel resolution, E is the energy, $F(E)$ is the differential energy flux, and i is the index of a given energy channel. For the SWEA data, we compute this sum for energies above 800 eV to best isolate H^- from other high flux populations (Jones et al., 2022). We repeat this computation for SWIA for energies spanning 300 to 4,000 eV in order to exclude spacecraft charging signatures in addition to pickup ions. Figure 9 summarizes our findings.

Recalling from Section 3.2.2, we anticipate 0.04 - 0.45% of upstream solar wind protons to be converted to H^+ (Halekas, 2017) and 0.0029 - 0.0234% to H^-. Panels B and C summarize the observed conversion efficiency for these populations, respectively. We see in Panel B that the conversion rate from solar wind protons to downstream H^+ is ∼0.8% across all energies, which is higher than the aforementioned anticipated limits. However, if we increase these limits by a factor of 3 to account for expansion of the hydrogen corona at perihelion (hashed region in Figure 9B), we find that the observed conversion rate aligns well with the model outlined in Halekas (2017). If we now look at the corresponding results in Panel C for H^-, we observe a ∼0.1% conversion rate, which is much higher than our derived limits. We do observe slight overlap between the lower limit

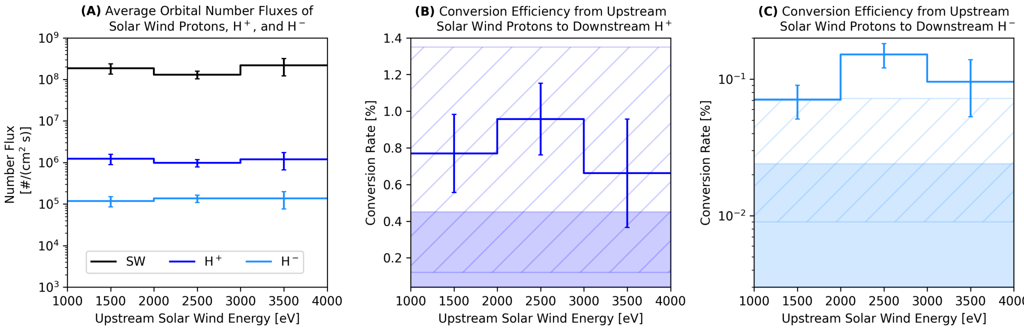

Figure 9. Summary of solar wind, H^+, and H^- orbital fluxes and corresponding conversion rates. (A) Orbit-averaged number fluxes for upstream solar wind protons (black), downstream H^+ (blue), and downstream H^- (light blue). Errorbars correspond to the standard error of the mean for a given bin. (B) Percent of solar wind protons converted to H^+. (C) Percent of solar wind protons converted to H^-. Shaded regions in B and C represent the percentage ranges based on our computations in Section 3.2.2 and previous findings (Kallio et al., 1997; Halekas, 2017). Hashed regions represent anticipated percentages at perihelion.

of our observations and the upper limit of the conversion rate at perihelion. This discrepancy between our model and observations may stem from an overestimation of σ_{20}. Smaller values of σ_{20} would result in larger values of F^- across all solar wind energies. Further investigation is required to better understand this behavior, and direct measurements of σ_{20} at solar wind energies would be extremely beneficial.

Examining Equation 26, we find that the turnover column densities for H^- and H^+ span $(3.068 \pm 0.059)\times10^{14}$ cm^{-2} and $(6.426 \pm 0.140)\times10^{14}$ cm^{-2} for energies falling between 1 and 3 keV, respectively (Nakai et al., 1987; Lindsay et al., 2005; Halekas, 2017). Comparing these values to the observed trends in Figure 5, we see that the observed profiles for both particle populations begin to plateau at these aforementioned column density values. This indicates that H^+ and H^- do approximately equilibrate after one e-folding scale, as was estimated by Equation 26.

We can also compare the observed abundance of H^+ with respect to H^- to what we would expect given the conversion rate of ENAs to each particle species. In Figure 5, we note that the peak ratio of H^+ to H^- fluxes in Panel C is $\sim$8. From our analysis in Section 3.2.2, we can determine the anticipated ratio of H^+ flux to H^- flux. We predicted that 0.29 - 0.78% of ENAs are converted to H^-, while Halekas (2017) determined that 4 - 15% of ENAs are converted to H^+. Using these limits, we can anticipate H^+ to be $\sim$13 - 19 times more abundant than H^-. These values are $\sim$2 times higher than the maximum observed ratio in Figure 5. This discrepancy is not surprising, given the conversion rates obtained in Figure 9. From our observations, we would anticipate a H^+/H^- ratio of $\sim$10, which is more in line with what we observe in Figure 5.

5 Summary

Using MAVEN data, we determine under what conditions H^- is best observed and compare fluxes of H^- and H^+ as a function of CO_2 column density. Using various methods, we isolate orbits with H^- signatures and determine that precipitation of this particle population is incredibly rare (1.8% of available observations). We also find that these particles are best observed during periods of high energy solar wind near perihelion; more of these events may become observable by MAVEN as we approach solar maximum, during which high energy solar events (i.e., CIRs, SIRs, CMEs) become more frequent. We observe no clear correlation between solar EUV irradiance or solar cycle with H^- observations. Lastly, we find that H^+ is preferentially generated from precipitating solar wind hydrogen ENAs compared to H^-. On average, H^+ fluxes are 4.5 times greater than observed H^- fluxes as a function of CO_2 column density.

We develop a simple model describing the equilibrium conditions for H^- in the Martian atmosphere by building off of a framework previously constructed by Halekas (2017). We consider the effects of charge exchange, electron attachment, and photodetachment in our model. We find numerical solutions for the charge (F^-) and neutral fractions (F^0) and determine the converging charge fraction to span 0.29 - 0.78% depending on upstream solar wind energy. We do not observe a significant change in the numerical solutions for F^- or F^0 between perihelion and aphelion. We find that the maximum difference between the analytical and numerical solutions when photodetachment is incorporated is 1 - 7%, occurring between 125 and 250 km.

When comparing our model to observations, we find good agreement in the equilibrium column densities for H^- and H^+. We observe a slight discrepancy in the observed charge fraction of H^- compared to our model, which underestimates our observations. We also find that the ratio of observed H^+/H^- fluxes is smaller than anticipated with our given model parameters. Further observations of H^- are needed to better understand the discrepancies discussed here.

Future work could compare the conditions under which we observe H^-, H^+, and proton aurora at Mars. Determining the distribution of these events will help us to better understand the Mars-solar wind interaction, as well as the primary factors governing the precipitation of hydrogen ENAs. The model describing H^- precipitation could also be expanded upon, accounting for hydrogen depletion caused by H^+ charge exchange with CO_2, seasonal variability of the hydrogen corona, as well as solar zenith angle dependencies. These two latter parameters greatly affect observed hydrogen deposition at Mars and are worth investigating (Halekas, 2017; Henderson et al., 2021; Hughes et al., 2019, 2023). It would also be of great scientific value to obtain direct measurements of electron stripping of H^- by CO_2 at solar wind energies to better constrain these processes as well.

6 Open Research

All MAVEN data utilized in this project are available on the NASA Planetary Data System. MAVEN SWIA data can be found here: `https://pds-ppi.igpp.ucla.edu/mission/MAVEN/MAVEN/SWIA`. MAVEN NGIMS data are available here: `https://pds-ppi.igpp.ucla.edu/mission/MAVEN/MAVEN/NGIMS`. MAVEN EUVM data are located here: `https://pds-ppi.igpp.ucla.edu/mission/MAVEN/MAVEN/EUV`. MAVEN SWEA data can be found at the following link: `https://pds-ppi.igpp.ucla.edu/mission/MAVEN/MAVEN/SWEA`. Photodetachment cross section data were curated by McLaughlin et al. (2017). Photoabsorption cross sections were obtained from multiple sources and can be found compiled at Henderson et al. (2023). Electron attachment cross sections can be found in Lindsay et al. (2005), and H^- charge exchange cross sections obtained in Section 3.2 can be found at Henderson et al. (2023). Solar wind data can also be found at Henderson et al. (2023).

Acknowledgments

The authors would like to acknowledge the MAVEN contract for support. We would also like to thank Dr. Casey DeRoo and Dr. Steve Spangler for their insightful conversations throughout this project.

References

Anderson Jr., D. E. (1974). Mariner 6, 7, and 9 Ultraviolet Spectrometer Experiment: Analysis of hydrogen Lyman alpha data. *Journal of Geophysical Research (1896-1977)*, *79*(10), 1513-1518. doi: https://doi.org/10.1029/JA079i010p01513

Bisikalo, D. V., Shematovich, V. I., Gérard, J.-C., & Hubert, B. (2018). Monte Carlo Simulations of the Interaction of Fast Proton and Hydrogen Atoms with the Martian Atmosphere and Comparison With In Situ Measurements. *Journal of Geophysical Research: Space Physics*, *123*(7), 5850-5861. doi: https://doi.org/10.1029/2018JA025400

Branscomb, L. M., & Smith, S. J. (1955, May). Experimental cross section for photodetachment of electrons from h^- and d^-. *Phys. Rev.*, *98*, 1028–1034. doi: 10.1103/PhysRev.98.1028

Brecht, S. H. (1997). Solar wind proton deposition into the Martian atmosphere. *Journal of Geophysical Research: Space Physics*, *102*(A6), 11287-11294. doi: https://doi.org/10.1029/97JA00561

Brinkfeldt, K., Gunell, H., Brandt, P. C., Barabash, S., Frahm, R., Winningham, J., ... Dierker, C. (2006). First ENA observations at Mars: Solar-wind ENAs on the nightside. *Icarus*, *182*(2), 439-447. (Results from the Mars Express ASPERA-3 Investigation) doi: https://doi.org/10.1016/j.icarus.2005.12.023

Cairns, R. B., & Samson, J. A. R. (1965). Absorption and photoionization cross sections of co2, co, ar, and he at intense solar emission lines. *Journal of Geophysical Research (1896-1977)*, *70*(1), 99-104. doi: https://doi.org/10.1029/JZ070i001p00099

Chaffin, M. S., Kass, D. M., Aoki, S., Fedorova, A. A., Deighan, J., Connour, K., ... Korablev, O. I. (2021, October). Martian water loss to space enhanced by regional dust storms. *Nature Astronomy*, *5*, 1036-1042. doi: 10.1038/s41550-021-01425-w

Chandrasekhar, S. (1945, September). On the Continuous Absorption Coefficient of the Negative Hydrogen Ion. *The Astrophysical Journal*, *102*, 223. doi: 10.1086/144755

Chaufray, J., Bertaux, J., Leblanc, F., & Quémerais, E. (2008). Observation of the hydrogen corona with SPICAM on Mars Express. *Icarus*, *195*(2), 598-613. doi: https://doi.org/10.1016/j.icarus.2008.01.009

Conrath, B., Curran, R., Hanel, R., Kunde, V., Maguire, W., Pearl, J., ... Burke, T. (1973). Atmospheric and surface properties of mars obtained by infrared spectroscopy on mariner 9. *Journal of Geophysical Research (1896-1977)*, *78*(20), 4267-4278. doi: https://doi.org/10.1029/JB078i020p04267

Cravens, T. E., Hamil, O., Houston, S., Bougher, S., Ma, Y., Brain, D., & Ledvina, S. (2017). Estimates of ionospheric transport and ion loss at Mars. *Journal of Geophysical Research: Space Physics*, *122*, 10626–10637. doi: https://doi.org/10.1002/2017JA024582

Craver, C. D. (1982). *The coblentz society desk book of infrared spectra.* (2nd ed. ed.). Kirkwood, MO: The Society.

Deighan, J., Jain, S. K., Chaffin, M. S., Fang, X., Halekas, J. S., Clarke, J. T., ... Jakosky, B. M. (2018, July). Discovery of a proton aurora at Mars. *Nature Astronomy*, *2*, 802-807. doi: 10.1038/s41550-018-0538-5

Desai, R. T., Zhang, Z., Wu, X., & Lue, C. (2021, may). Photodetachment and test-particle simulation constraints on negative ions in solar system plasmas. *The Planetary Science Journal*, *2*(3), 99. doi: 10.3847/PSJ/abf638

Diéval, C., Kallio, E., Barabash, S., Stenberg, G., Nilsson, H., Futaana, Y., ... Brain, D. A. (2012). A case study of proton precipitation at Mars: Mars Express observations and hybrid simulations. *Journal of Geophysical Research: Space Physics*, *117*(A6). doi: https://doi.org/10.1029/2012JA017537

Eparvier, F., Chamberlin, P., & Woods, T. (2015). The Solar Extreme Ultraviolet

Monitor for MAVEN. *Space Sci Rev*, *195*, 293–301. doi: https://doi.org/10.1007/s11214-015-0195-2

Futaana, Y., Barabash, S., Grigoriev, A., Holmström, M., Kallio, E., Brandt, P. C., … Dierker, C. (2006a). First ENA observations at Mars: ENA emissions from the Martian upper atmosphere. *Icarus*, *182*(2), 424-430. (Results from the Mars Express ASPERA-3 Investigation) doi: https://doi.org/10.1016/j.icarus.2005.09.019

Futaana, Y., Barabash, S., Grigoriev, A., Holmström, M., Kallio, E., Brandt, P. C., … Dierker, C. (2006b). First ENA observations at Mars: Subsolar ENA jet. *Icarus*, *182*(2), 413-423. (Results from the Mars Express ASPERA-3 Investigation) doi: https://doi.org/10.1016/j.icarus.2005.08.024

Girazian, Z., & Halekas, J. (2021). Precipitating Solar Wind Hydrogen at Mars: Improved Calculations of the Backscatter and Albedo With MAVEN Observations. *Journal of Geophysical Research: Planets*, *126*(2), e2020JE006666. (e2020JE006666 2020JE006666) doi: https://doi.org/10.1029/2020JE006666

Gunell, H., Brinkfeldt, K., Holmström, M., Brandt, P. C., Barabash, S., Kallio, E., … Dierker, C. (2006). First ENA observations at Mars: Charge exchange ENAs produced in the magnetosheath. *Icarus*, *182*(2), 431-438. (Results from the Mars Express ASPERA-3 Investigation) doi: https://doi.org/10.1016/j.icarus.2005.10.027

Halekas, J. S. (2017). Seasonal variability of the hydrogen exosphere of Mars. *Journal of Geophysical Research: Planets*, *122*(5), 901-911. doi: https://doi.org/10.1002/2017JE005306

Halekas, J. S., Lillis, R. J., Mitchell, D. L., Cravens, T. E., Mazelle, C., Connerney, J. E. P., … Ruhunusiri, S. (2015). MAVEN observations of solar wind hydrogen deposition in the atmosphere of Mars. *Geophysical Research Letters*, *42*(21), 8901-8909. doi: https://doi.org/10.1002/2015GL064693

Halekas, J. S., Ruhunusiri, S., Harada, Y., Collinson, G., Mitchell, D. L., Mazelle, C., … Jakosky, B. M. (2017). Structure, dynamics, and seasonal variability of the Mars-solar wind interaction: MAVEN Solar Wind Ion Analyzer in-flight performance and science results. *Journal of Geophysical Research: Space Physics*, *122*(1), 547-578. doi: https://doi.org/10.1002/2016JA023167

Halekas, J. S., Taylor, E. R., Dalton, G., Johnson, G., Curtis, D. W., McFadden, J. P., … Jakosky, B. M. (2015). The Solar Wind Ion Analyzer for MAVEN. *Space Science Reviews*, *195*(1-4), 125-151. doi: 10.1007/s11214-013-0029-z

Henderson, S., Halekas, J., Girazian, Z., Espley, J., & Elrod, M. (2022). Influence of Magnetic Fields on Precipitating Solar Wind Hydrogen at Mars. *Geophysical Research Letters*, *49*(12), e2022GL099114. (e2022GL099114 2022GL099114) doi: https://doi.org/10.1029/2022GL099114

Henderson, S., Halekas, J., Jolitz, R., Mitchell, D., Mazelle, C., Eparvier, F., & Elrod, M. (2023). *MAVEN H^- Data (2014-2023).* Zenodo. doi: 10.5281/zenodo.8422352

Henderson, S., Halekas, J., Lillis, R., & Elrod, M. (2021). Precipitating Solar Wind Hydrogen as Observed by the MAVEN Spacecraft: Distribution as a Function of Column Density, Altitude, and Solar Zenith Angle. *Journal of Geophysical Research: Planets*, *126*(7), e2020JE006725. (e2020JE006725 2020JE006725) doi: https://doi.org/10.1029/2020JE006725

Holmström, M., Barabash, S., & Kallio, E. (2002). Energetic neutral atoms at Mars 1. Imaging of solar wind protons. *Journal of Geophysical Research: Space Physics*, *107*(A10). doi: https://doi.org/10.1029/2001JA000325

Huebner, W. F., Keady, J. J., & Lyon, S. P. (1992, September). Solar Photo Rates for Planetary Atmospheres and Atmospheric Pollutants. , *195*(1), 1-294. doi: 10.1007/BF00644558

Huebner, W. F., & Mukherjee, J. (2015, February). Photoionization and photodissociation rates in solar and blackbody radiation fields. , *106*, 11-45. doi:

10.1016/j.pss.2014.11.022
Hughes, A., Chaffin, M., Mierkiewicz, E., Deighan, J., Jain, S., Schneider, N., ... Jakosky, B. (2019). Proton Aurora on Mars: A Dayside Phenomenon Pervasive in Southern Summer. *Journal of Geophysical Research: Space Physics*, *124*(12), 10533-10548. doi: https://doi.org/10.1029/2019JA027140
Hughes, A., Chaffin, M., Mierkiewicz, E., Deighan, J., Jolitz, R., Kallio, E., ... Hegyi, B. (2023). Advancing Our Understanding of Martian Proton Aurora through a Coordinated Multi-Model Comparison Campaign. *Journal of Geophysical Research: Space Physics*.
Jakosky, B., Lin, R., & Grebowsky, J. e. a. (2015). The Mars Atmosphere and Volatile Evolution (MAVEN) Mission. *Space Science Reviews*, *195*, 3-48. doi: https://doi.org/10.1007/s11214-015-0139-x
Jones, N., Halekas, J., Girazian, Z., Mitchell, D., & Mazelle, C. (2022). MAVEN Observations of H^- Ions in the Martian Atmosphere. *Journal of Geophysical Research: Planets*, *127*(6), e2021JE006999. (e2021JE006999 2021JE006999) doi: https://doi.org/10.1029/2021JE006999
Kallio, E., & Barabash, S. (2000). On the elastic and inelastic collisions between precipitating energetic hydrogen atoms and martian atmospheric neutrals. *Journal of Geophysical Research: Space Physics*, *105*(A11), 24973-24996. doi: https://doi.org/10.1029/2000JA900077
Kallio, E., & Barabash, S. (2001). Atmospheric effects of precipitating energetic hydrogen atoms on the Martian atmosphere. *Journal of Geophysical Research: Space Physics*, *106*(A1), 165-177. doi: https://doi.org/10.1029/2000JA002003
Kallio, E., Barabash, S., Brinkfeldt, K., Gunell, H., Holmström, M., Futaana, Y., ... Dierker, C. (2006). Energetic Neutral Atoms (ENA) at Mars: Properties of the hydrogen atoms produced upstream of the martian bow shock and implications for ENA sounding technique around non-magnetized planets. *Icarus*, *182*(2), 448-463. (Results from the Mars Express ASPERA-3 Investigation) doi: https://doi.org/10.1016/j.icarus.2005.12.019
Kallio, E., Luhmann, J. G., & Barabash, S. (1997). Charge exchange near Mars: The solar wind absorption and energetic neutral atom production. *Journal of Geophysical Research: Space Physics*, *102*(A10), 22183-22197. doi: https://doi.org/10.1029/97JA01662
Lewis, B., & Carver, J. (1983). Temperature dependence of the carbon dioxide photoabsorption cross section between 1200 and 1970 Å. *Journal of Quantitative Spectroscopy and Radiative Transfer*, *30*(4), 297-309. doi: https://doi.org/10.1016/0022-4073(83)90027-4
Lindsay, B. G., Yu, W. S., & Stebbings, R. F. (2005, Mar). Cross sections for charge-changing processes involving kilo-electron-volt H and H^+ with CO and CO_2. *Phys. Rev. A*, *71*, 032705. doi: 10.1103/PhysRevA.71.032705
Mahaffy, P., Benna, M., & King, T. e. a. (2015). The Neutral Gas and Ion Mass Spectrometer on the Mars Atmosphere and Volatile Evolution Mission. *Space Science Reviews*, *195*, 49-73. doi: https://doi.org/10.1007/s11214-014-0091-1
Mahaffy, P. R., Benna, M., Elrod, M., Yelle, R. V., Bougher, S. W., Stone, S. W., & Jakosky, B. M. (2015). Structure and composition of the neutral upper atmosphere of Mars from the MAVEN NGIMS investigation. *Geophysical Research Letters*, *42*(21), 8951-8957. doi: https://doi.org/10.1002/2015GL065329
McLaughlin, B. M., Stancil, P. C., Sadeghpour, H. R., & Forrey, R. C. (2017, may). H photodetachment and radiative attachment for astrophysical applications. *Journal of Physics B: Atomic, Molecular and Optical Physics*, *50*(11), 114001. doi: 10.1088/1361-6455/aa6c1f
Mitchell, D., Mazelle, C., & Sauvaud, J. e. a. (2016). The MAVEN Solar Wind Electron Analyzer. *Space Science Reviews*, *200*, 495-528. doi: https://doi.org/10.1007/s11214-015-0232-1
Mitchell, D. L., Lin, R. P., Mazelle, C., Rème, H., Cloutier, P. A., Connerney,

J. E. P., ... Ness, N. F. (2001). Probing Mars' crustal magnetic field and ionosphere with the MGS Electron Reflectometer. *Journal of Geophysical Research: Planets*, *106*(E10), 23419-23427. doi: https://doi.org/10.1029/2000JE001435

Nakai, Y., Shirai, T., Tabata, T., & Ito, R. (1987). Cross sections for charge transfer of hydrogen atoms and ions colliding with gaseous atoms and molecules. *Atomic Data and Nuclear Data Tables*, *37*(1), 69-101. doi: https://doi.org/10.1016/0092-640X(87)90005-2

Nier, A. O., & McElroy, M. B. (1977). Composition and structure of Mars' Upper atmosphere: Results from the neutral mass spectrometers on Viking 1 and 2. *Journal of Geophysical Research (1896-1977)*, *82*(28), 4341-4349. doi: https://doi.org/10.1029/JS082i028p04341

Parkinson, W., Rufus, J., & Yoshino, K. (2003). Absolute absorption cross section measurements of co2 in the wavelength region 163–200 nm and the temperature dependence. *Chemical Physics*, *290*(2), 251-256. doi: https://doi.org/10.1016/S0301-0104(03)00146-0

Rahman, F., & Hird, B. (1986). Electron detachment atomic cross sections from negative ions. *Atomic Data and Nuclear Data Tables*, *35*(1), 123-183. doi: https://doi.org/10.1016/0092-640X(86)90029-X

Ritter, B., Gérard, J.-C., Hubert, B., Rodriguez, L., & Montmessin, F. (2018). Observations of the proton aurora on mars with spicam on board mars express. *Geophysical Research Letters*, *45*(2), 612-619. doi: https://doi.org/10.1002/2017GL076235

Shematovich, V., & Bisikalo, D. (2021). A Kinetic Model for Precipitation of Solar-Wind Protons into the Martian Atmosphere. *Astronomy Reports*, *65*, 869-875. doi: https://doi.org/10.1134/S106377292110036X

Shematovich, V. I., Bisikalo, D. V., Diéval, C., Barabash, S., Stenberg, G., Nilsson, H., ... Gérard, J.-C. (2011). Proton and hydrogen atom transport in the Martian upper atmosphere with an induced magnetic field. *Journal of Geophysical Research: Space Physics*, *116*(A11). doi: https://doi.org/10.1029/2011JA017007

Smith, S. J., & Burch, D. S. (1959, Feb). Photodetachment cross section of the negative hydrogen ion. *Phys. Rev. Lett.*, *2*, 165–166. doi: 10.1103/PhysRevLett.2.165

Stark, G., Yoshino, K., Smith, P., & Ito, K. (2007). Photoabsorption cross section measurements of co2 between 106.1 and 118.7nm at 295 and 195k. *Journal of Quantitative Spectroscopy and Radiative Transfer*, *103*(1), 67-73. doi: https://doi.org/10.1016/j.jqsrt.2006.07.001

Stone, S. W., Yelle, R. V., Benna, M., Elrod, M. K., & Mahaffy, P. R. (2018). Thermal Structure of the Martian Upper Atmosphere From MAVEN NGIMS. *Journal of Geophysical Research: Planets*, *123*(11), 2842-2867. doi: https://doi.org/10.1029/2018JE005559

Sun, H., & Weissler, G. L. (1955, 12). Absorption Cross Sections of Carbon Dioxide and Carbon Monoxide in the Vacuum Ultraviolet. *The Journal of Chemical Physics*, *23*(9), 1625-1628. doi: 10.1063/1.1742398

Wang, X.-D., Alho, M., Jarvinen, R., Kallio, E., Barabash, S., & Futaana, Y. (2018). Precipitation of Hydrogen Energetic Neutral Atoms at the Upper Atmosphere of Mars. *Journal of Geophysical Research: Space Physics*, *123*(10), 8730-8748. doi: https://doi.org/10.1029/2018JA025188

Wang, X.-D., Barabash, S., Futaana, Y., Grigoriev, A., & Wurz, P. (2013). Directionality and variability of energetic neutral hydrogen fluxes observed by Mars Express. *Journal of Geophysical Research: Space Physics*, *118*(12), 7635-7642. doi: https://doi.org/10.1002/2013JA018876

Wishart, A. W. (1979, November). The bound-free photodetachment cross section of h-. *Journal of Physics B: Atomic and Molecular Physics*, *12*(21), 3511. doi: 10.1088/0022-3700/12/21/009

Yoshino, K., Esmond, J., Sun, Y., Parkinson, W., Ito, K., & Matsui, T. (1996). Absorption cross section measurements of carbon dioxide in the wavelength region 118.7–175.5 nm and the temperature dependence. *Journal of Quantitative Spectroscopy and Radiative Transfer*, *55*(1), 53-60. doi: https://doi.org/10.1016/0022-4073(95)00135-2

Journal of Geophysical Research: Space Physics

Supporting Information for

Characterizing Precipitation Behaviors of H^- in the Martian Atmosphere

Sarah Henderson[1,2], Jasper Halekas[1], Rebecca Jolitz[3], David Mitchell[3], Christian Mazelle[4], Frank Eparvier[5], Meredith Elrod[6]

[1] The University of Iowa, Iowa City, IA, USA
[2] Montana State University, Bozeman, MT, USA
[3] Space Sciences Laboratory, University of California Berkeley, Berkeley, CA, USA
[4] IRAP, Université de Toulouse, CNRS, UPS, CNES, Toulouse, France
[5] Laboratory for Atmospheric and Space Physics, University of Colorado, Boulder, CO, USA
[6] Planetary Environments Lab, Goddard Space Flight Center, NASA, Greenbelt, MD, USA
[7] CRESST II, University of Maryland, College Park, College Park, MD, USA

Contents of this file

Figures S1, S2, and S3.

Introduction

This supporting document includes figures outlining parameters implemented in various calculations throughout our manuscript. Here, we include a plot summarizing photodetachment and photoabsorption cross section curves as a function of energy. These values were utilized in our calculations in Section 3.1. We also include an average CO_2 profile derived from dayside, inbound verified NGIMS data. We fit an exponentially decaying function to these average data and note the fitting parameters (N_0 and m) in our plot. These fit parameters were implemented in calculations in Sections 3.2, 3.2.1, and 3.2.2. We also include a summary of the differences between the numerical modeling results discussed in Section 3.2 at different Mars-Sun distances.

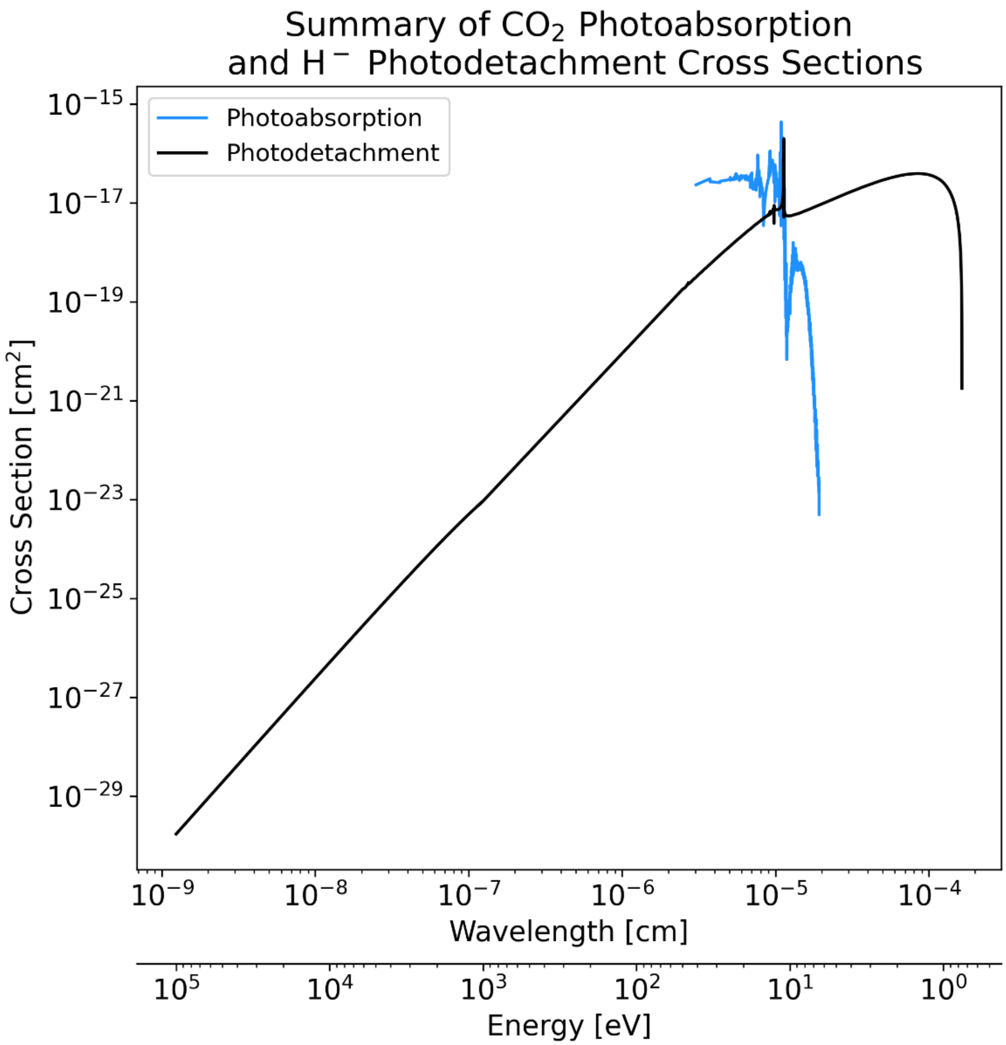

Figure S1. Summary of CO_2 photoabsorption and H^- photodetachment cross sections. EUV photoabsorption cross sections compiled from numerous sources (Sun & Weissler, 1955; Cairns & Samson, 1965; Lewis & Carver, 1983; Yoshino et al., 1996; Parkinson et al., 2003; Stark et al., 2007). Photodetachment cross sections from McLaughlin et al. (2017) and sources therein.

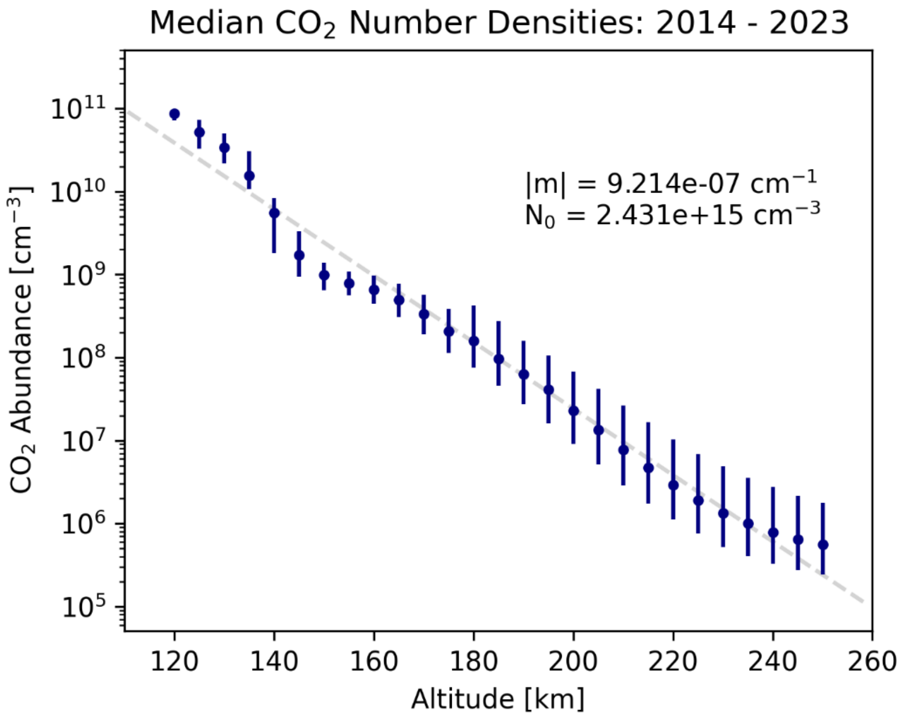

Figure S2. Median CO_2 density profile from inbound verified dayside NGIMS data collected between 2014 and 2023 with interquartile ranges Q1 and Q3 as lower and upper error bars, respectively. Fit parameters, N_0 and m, are in the upper right corner. Resulting fit overplotted in gray, dashed line.

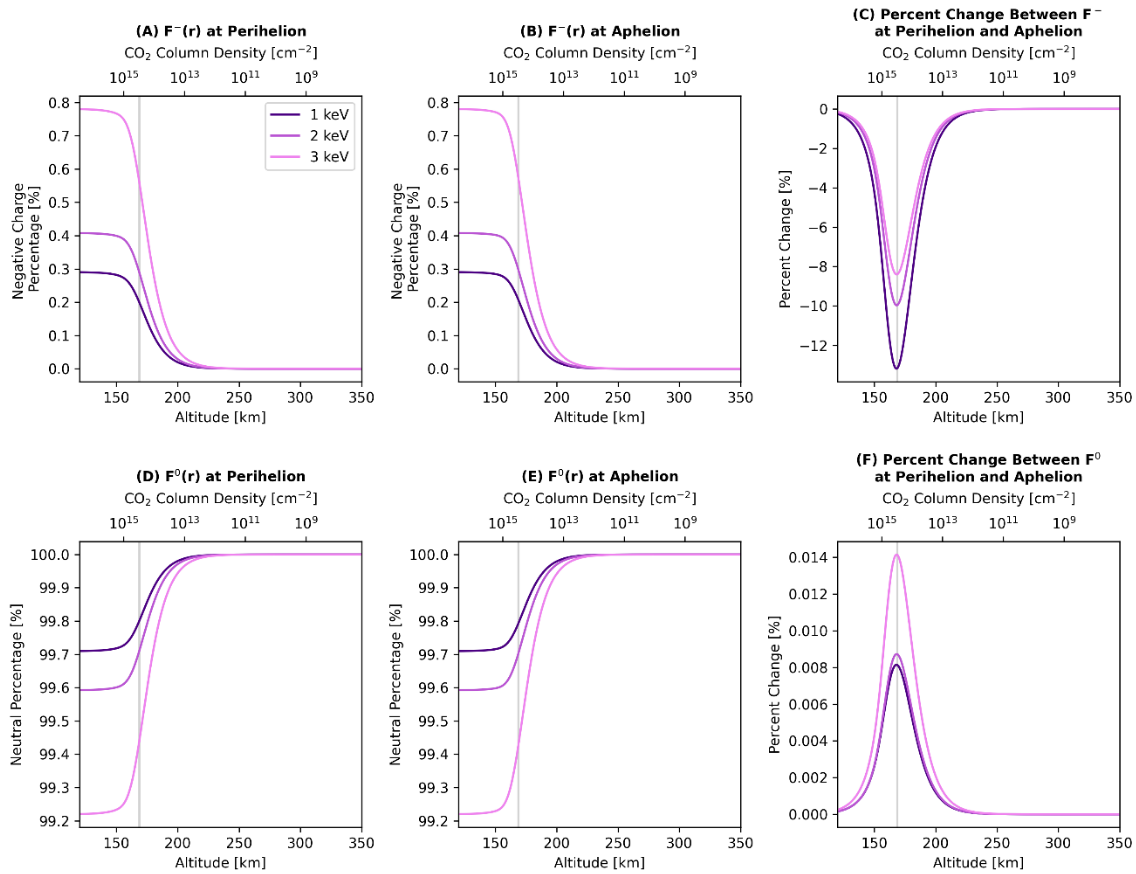

Figure S3. Summary of numerical solutions to Equations 19 and 20 at different Mars-Sun distances. (A) Negative charge fraction (F^-) versus altitude and column density for upstream solar wind energies of 1, 2, and 3 keV at perihelion. (B) Same as Panel A but at aphelion. (C) Percent change ($c = 100\ [F^-_{PER}-F^-_{AP}]/\ F^-_{AP}$) between F^- at perihelion and aphelion for each solar wind energy. Panels D - F follow this format but display the neutral fraction (F^0) solutions. Gray vertical region in each subpanel highlights the equilibrium column density range (i.e., where one e-folding occurs in Equations 27 and 28). It should be noted that no atmospheric changes between aphelion and perihelion were incorporated in these results; only the changes induced by the Mars-Sun distance dependence in Equations 19 and 20 are displayed here.